Accepted Manuscript

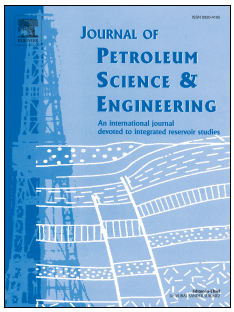

Numerical considerations for the simulation of proppant transport through fractures

Endrina Rivas, Robert Gracie

PII: S0920-4105(19)30518-2

DOI: https://doi.org/10.1016/j.petrol.2019.05.064

Reference: PETROL 6113

To appear in: *Journal of Petroleum Science and Engineering*

Received Date: 5 March 2019

Revised Date: 13 May 2019

Accepted Date: 27 May 2019

Please cite this article as: Rivas, E., Gracie, R., Numerical considerations for the simulation of proppant transport through fractures, *Journal of Petroleum Science and Engineering* (2019), doi: https://doi.org/10.1016/j.petrol.2019.05.064.

Numerical Considerations for the Simulation of Proppant Transport Through Fractures

Endrina Rivas[a], Robert Gracie[a,*]

[a]*Department of Civil and Environmental Engineering, University of Waterloo, Waterloo, Ontario, N2L 3G1, Canada*

Abstract

Injection of a proppant slurry (fluid mixed with granular material) into a reservoir to keep fractures open is a common procedure in hydraulic fracturing treatments. This article presents the numerical methodology for simulation of proppant transport through a hydraulic fracture using the Finite Volume Method. Proppant models commonly used in the hydraulic fracture literature solve the linearized advection equation; this work presents solution methods for the nonlinear form of the proppant flux equation.

The complexities of solving the nonlinear hyperbolic advection equation that governs proppant transport are tackled, particularly handling shock waves that are generated due to the nonlinear flux function and the spatially-varying width and pressure gradient along the fracture. A critical time step is derived for the proppant transport problem solved using an explicit solution strategy. A predictor-corrector algorithm is developed to constrain the proppant from exceeding the physically admissible range. The model is able to capture the mechanism of proppant bridging which occurs in sections of narrow fracture width, tip screen-out which occurs where fracture becomes saturated with proppant, and flushing of proppant into new fracture segments. The results are verified by comparing with characteristic solutions, and the model is used to simulate proppant transport through a KGD fracture.

Declarations of interest: none

Keywords: Proppant transport, Hydraulic fracture, Proppant bridging, Multiphase Flow, Nonlinear advection, Finite volume

1. Introduction

Hydraulic fracturing (HF) is a reservoir stimulation treatment that increases rock permeability by the injection of high-pressure fluid into a formation. In HF treatments, proppant (granular material, typically sand) is injected into the wellbore to keep the fracture network open after pumping ceases. Proppant usage worldwide has increased drastically since 2009, with close to 92 billion pounds of proppant pumped in 2013 [1]. The final position of the slurry–the mixture of wellbore fluids and proppant–in the fracture network following injection plays a large role in determining the final permeability of the treated volume. Simulation of proppant transport through a fracture is a topic of research that can lead to a better understanding of the permeability increase and ultimately help guide the design of the hydraulic fracturing treatment. A review of the geomechanics and numerical methods used in modeling hydraulic fracturing is provided by Adachi et al. [2], Detournay [3], Hattori et al. [4], and Lecampion et al. [5].

Of the various mechanisms involved in hydraulic fracturing, the focal point of this paper is on the transport of proppant through hydraulic fractures. An extensive review of the fluid mechanics associated with the multiphase flow in hydraulic fracturing has been performed by Osiptsov [6]. Early researchers tackled the problem of modelling proppant transport using simplified models to find the position of proppant over

*Corresponding author
Email address: rgracie@uwaterloo.ca (Robert Gracie)

time through a stationary channel and focused on the mechanism of proppant settling towards the bottom of the channel [7, 8]. Mixture models have also been used, which are a more general model that solve for the conservation of mass of the slurry and the proppant to advance the proppant concentration [2, 9–12]. These models assume that the phases are fully mixed and treat the slurry as a fluid with a modified viscosity and density based on the concentration of proppant. The fluid and proppant are assumed to be incompressible and the fracture width is assumed to be small enough compared to the other fracture dimensions that lubrication theory holds. The most basic form of the mixture model assumes that the slurry components (fluid and proppant particles) travel at the same velocity. The difference in velocity between the slurry and the proppant particles has been considered by some authors, but in most models only slip along the height of the fracture due to convection and settlement is accounted for. A notable exception is the model by Dontsov and Peirce [13], which provides a slip related to Darcy flow of fluid through the proppant pack once the proppant concentration reaches a saturated level. Two-phase modelling of proppant transport has also been approached [14], in which both the conservation of momentum and mass are solved for the fluid and the proppant particles. This type of model provides a deeper understanding of the interaction between the two phases but is computationally expensive.

A mixture model is considered in this paper due to its efficiency and ease of implementation with other reservoir models. There are three governing equations that are typically solved for in hydraulic fracture simulations: (I) conservation of momentum governing rock deformation, (II) conservation of mass governing slurry flow, and (III) conservation of mass governing proppant flow. The second equation inherently incorporates the conservation of mass of the carrier fluid. These three equations are used to solve for the rock mass displacement, fluid pressure, and proppant concentration, respectively. All equations are functions of the three independent variables and are strongly coupled in terms of the physical processes involved. Many models in the literature solve the rock deformation (I) and slurry flow (II) equations simultaneously in a monolithic scheme (i.e., strongly coupled), using the proppant concentration from the previous time step[2, 10–12, 15]. Once a converged solution is obtained for the fracture width and slurry pressure, the proppant transport equation (III) is then solved to update the proppant concentration for the next time step while holding the fracture width and fluid velocity constant. The proppant update is considered a sequential coupling algorithm. However, most of these models don't iterate to obtain a converged solution for each step of the analysis, yielding a loosely coupled scheme which may lead to inaccuracies in the final solution.

The focus of this paper is on the solution of the proppant transport equation (III), keeping in mind its solution as a part of a sequentially coupled HF solution. The continuity equation that governs the proppant flow through the fracture is a nonlinear hyperbolic advection equation. The advection equation has been solved in hydraulic fracture models using the finite volume method [10, 11, 16–18], the finite difference method [12, 15], and the finite element method [9]. Most models are solved using an Eulerian frame of reference, but a solution using a Lagrangian frame of reference is also possible [19]. The coupled mixture models in the literature assume a constant slurry velocity during the proppant transport update, which often leads to a linear advection equation. Finite volume schemes have been used to solve nonlinear advection of proppant in a hydraulic fracture [11, 16], although the slurry velocity is also held constant during the solution of the proppant transport equation in these models. Finite volume schemes have also been used by various researchers to model nonlinear hyperbolic equations in similar fields, such as the work by Varadarajan and Hammond [20] in modeling gas migration and Lorentzen and Fjelde [21] in modeling multiphase hydrocarbon flow in pipelines. Numerically, solving the nonlinear equation presents additional challenges due to the shocks created in the solution that must be considered in the approximation. Oscillations may be introduced into the solution if the characteristic speed at the cell edges is not properly approximated. An entropy correction must be included in the formulation to handle rarefaction waves. Additionally, proppant concentration constraints must be imposed on the solution so that the approximation does not lead to results that are outside the physically possible limits since this is not handled naturally by the governing equation.

The purpose of this paper is to present the numerical methodology for solving the nonlinear hyperbolic partial differential equation that describes proppant transport through a hydraulic fracture in one-dimension using the finite volume method. A critical time step for the explicit nonlinear advection problem is derived for the proppant transport problem which works for all variations of the flux function. The methodology presented uses a new predictor-corrector algorithm to constrain the proppant from exceeding the physically

admissible range. Additionally, an application specific parameter that avoids introducing oscillations is found which is used to identify where the solution is smooth or discontinuous in approximating the characteristic speed at cell edges. The one-dimensional model presented in this paper is not able to capture all the relevant phenomena associated with proppant transport, such as settling, proppant bed formation, dune transport, and viscous fingering. The model can capture the shock waves generated due to the nonlinear flux function, and the effects of spatially-varying width and pressure gradient along the fracture. It can also capture the mechanism of proppant bridging, or the impediment of proppant flow when the fracture width is too narrow. The numerical methodology presented may be applied to a two-dimensional to capture other mechanisms of interest.

The governing equations for the proppant particle transport are derived in Section 2. Possible flux functions are described in this section. In Section 3, the Finite Volume Method is used to discretize the governing equations and the approximation of the finite volume fluxes is presented. This section includes the derivation of a critical time step for proppant transport, a discussion of the source of shocks in the nonlinear problem, the approximation of the characteristic speed and flux at the cell edges, and the boundary conditions imposed on the solution. A new algorithm for constraining the proppant concentration below the saturation limit is described in this section as well. Various numerical results are then discussed in Section 4, including proppant transport at the inlet, at a plug, through an elliptical fracture, and through a plane-strain KGD fracture. The solution is verified by comparing with characteristic solutions. Solutions are presented using a variety of effective viscosity expressions from the literature. The maximum injection rate permissible before proppant builds up and plugs at the fracture inlet is found, and the efficacy of the new constraint algorithm is studied. Conclusions are presented in the last section of the article.

2. Governing equations

The governing equation for proppant transport in a fracture is described in this section and placed in the context of the slurry (fluid and proppant mixture) flow. A mixture model is used which assumes that the fluid and proppant phases are fully mixed and that there is an equilibrium in mass, momentum and energy transfer [2]. Consider a two-dimensional fracture plane with a reference coordinate system, x, running along the length of the fracture at the centerline from the wellbore to the fracture tip, as depicted in Figure 1. The width of the fracture, $w(x)$, is described along the fracture length and the fracture height is assumed to extend a large distance into the domain, such that plane strain conditions apply. Assuming symmetry, only half of the fracture is modeled, with the point closest to the wellbore (or inlet) located at x_0 and the tip of the fracture at x_{tip}.

2.1. Slurry equations

The equations for conservation of mass for the proppant and fluid phase, respectively, are given in Equations (1) and (2) below. Summing these equations leads to the conservation of mass for the slurry, given in Equation (3).

$$\text{proppant mass}: \quad \frac{\partial}{\partial t}\left(\phi w \rho_p\right) + \frac{\partial Q_p(\phi, w, p_{,x})}{\partial x} = \phi_{inj} Q_{inj} \delta(x - x_0) \tag{1}$$

$$\text{fluid mass}: \quad \frac{\partial}{\partial t}\left((1-\phi) w \rho_f\right) + \frac{\partial Q_f(\phi, w, p_{,x})}{\partial x} + Q_{sink} = (1-\phi_{inj}) Q_{inj} \delta(x - x_0) \tag{2}$$

$$\text{slurry mass}: \quad \frac{\partial (w\rho)}{\partial t} + \frac{\partial Q(\phi, w, p_{,x})}{\partial x} + Q_{sink} = Q_{inj} \delta(x - x_0) \tag{3}$$

In these equations, $\phi(x,t)$ is the average volumetric concentration of proppant particles across the fracture width at time t. The density of the proppant particles and fluid, respectively, are given by ρ_p and ρ_f, while the density of the slurry is $\rho = \phi\rho_p + (1-\phi)\rho_f$. The mass flux of the proppant and fluid per unit fracture height are denoted by Q_p and Q_f, respectively. The total mass flux of the slurry, $Q = Q_p + Q_f$, is the

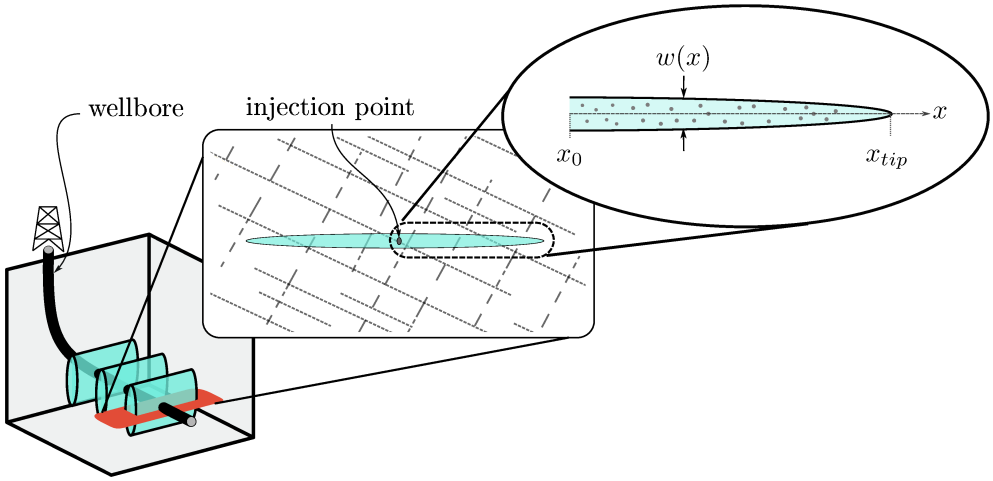

Figure 1: Domain of interest for proppant transport model is along the centerline of a horizontal plane of a vertical fracture

sum of the proppant and fluid mass fluxes. A constitutive law defines the relationship between the flux and pressure gradient of the slurry, $\partial p/\partial x$, described in further detail below. The source term, Q_{inj}, is the mass flux of slurry per unit area of fracture injected at the wellbore, x_0. The sink term, Q_{sink}, accounts for fluid leaving the fracture in the form of leak-off into the formation.

Any two of the equations (1)-(3) can be solved to obtain the unknown variables: fluid pressure, p, and proppant concentration, ϕ. Mixture models used to simulate hydraulic fractures in the literature typically solve the proppant (1) and slurry (3) conservation equations along with the elasticity equation that describes rock deformation to obtain the fracture width. In these models, the converged solution of the rock deformation and slurry flow is obtained first and then the proppant conservation law is used to update the concentration for the next time step.

The missing equation is a constitutive law which relates the mass flux to the concentration and pressure gradient. The most commonly used assumption is that of Poiseuille flow, with a correction for the viscosity of the slurry that is dependent on the proppant concentration, $\mu(\phi)$, described in further detail in Section 2.3. Hammond [22] defines these constitutive laws assuming both a homogeneous slurry and a close-packed core sheet. In this work, a homogeneous slurry is assumed. Solving the conservation of momentum of the slurry mixture using lubrication theory, the slurry velocity, v, as a function of the distance along the fracture width, y, is obtained,

$$v = \frac{1}{2\mu(\phi)} \frac{\partial p}{\partial x} \left(y^2 - yw\right) \tag{4}$$

The velocity of the proppant component of the slurry, v_p, is defined by assuming a slip velocity between the slurry and the proppant, $v^{slip} = v_p - v$. In the literature, this slip velocity has been related to proppant settling but most models do not include slip in the direction of the fracture length. In the context of the one-dimensional model used for this work, the proppant is assumed to flow with the same velocity as the slurry ($v_p = v$). The mass flux of the slurry, Q, and the proppant, Q_p, are defined respectively as

$$Q = \int_0^w \rho v dy = -\rho \frac{w^3}{12\mu(\phi)} \frac{\partial p}{\partial x} \tag{5}$$

$$Q_p = \int_0^w \phi \rho_p v_p dy = -\phi \rho_p \frac{w^3}{12\mu(\phi)} \frac{\partial p}{\partial x} \tag{6}$$

Coupled HF models in the literature typically hold the slurry velocity, v, constant during the proppant update, neglecting its dependence on the proppant equation as shown in Equation 4. Therefore, in these models the mass flux of the slurry is linearized to $Q_p = \phi w \rho_p v$. The work in this paper does not make this assumption, maintaining the nonlinear form of the proppant flux.

2.2. Proppant equation

The focus of this paper is solely on the solution of the continuity equation of the proppant. The specific form of the equation depends on the assumptions made about the effective viscosity of the slurry, which is described in further detail in the following section. The mass form of conservation equation (1) is rewritten in volumetric form for incompressible proppant as

$$\boxed{\frac{\partial(\phi w)}{\partial t} + \frac{\partial q}{\partial x} = \phi_{inj} q_{inj} \delta(x - x_0)} \tag{7}$$

where $q = Q_p/\rho_p$ is the volumetric flux of the proppant per unit height of the fracture and q_{inj} is the volumetric injection flux per unit area of the channel. The aim of this work is to discuss the solution of the nonlinear advection equation (7) for proppant flow in a fracture. Dividing equation (6) by the proppant density, the volumetric flux of the proppant is given as

$$q(\phi, \mu(\phi), w, p_{,x}) = -\phi \frac{w^3}{12\mu(\phi)} \frac{\partial p}{\partial x} \tag{8}$$

In this paper, the fracture width, $w(x,t)$, and the pressure gradient, $\partial p(x,t)/\partial x$, along the fracture length are assumed to be known values taken from the solution of the rock deformation and slurry flow equations, as would occur in a sequential solution to the HF model. The independent variable is the average proppant concentration, ϕ. In the context of the loosely-coupled models in the literature, this work is focused on the proppant update, excluding the solution of the solid and slurry equations. Since the effective viscosity, $\mu(\phi)$, is a function of the proppant concentration, substituting the constitutive law for the flux (8) into (7) leads to a nonlinear advection equation.

2.3. Flux functions

Various expressions have been postulated for the effective viscosity of the slurry as a function of the proppant concentration, $\mu(\phi)$. The first viscosity expression was proposed by Einstein [23], but is applicable only for dilute suspensions. Later expressions were proposed which represent a range of slurries, from dilute to saturated suspensions. Several commonly used expressions, with both theoretical and experimental origins, are provided in Table 1. These expressions are written in terms of the viscosity of the carrier fluid, μ_0. Many other functions have been proposed in the literature. A comparison of expressions for effective viscosity in the context of dense suspensions is given by Stickel and Powell [24].

The fully saturated concentration, ϕ_m, is defined as the maximum packing fraction of the proppant. This is the upper limit of physically allowable proppant concentration in a fracture. Values of saturated concentration in the literature range from 0.52 for loose-packed spheres [25] to 0.74 for hexagonal close-packing of monodisperse spherical particles [26]. In this work, a value of 0.64 is used, which is the value for random close-packing of monodisperse spherical particles [26].

The proppant flux associated with several of the expressions for effective viscosity from Table 1 for a range of normalized proppant concentration, ϕ/ϕ_m, between 0 and 1 are shown in Figure 2. The curves are defined using a saturated proppant concentration of 0.64, a carrier fluid viscosity of 1 mPa·s, a fracture width of 1 mm, and a pressure gradient of -1 kPa/m. These effective viscosities share the property that as the proppant concentration approaches zero, the effective viscosity approaches the viscosity of the carrier fluid. This limit describes pure fluid flow and the proppant flux also goes to zero at this limit.

At the limit where the proppant concentration reaches the saturation point, the proppant flux should also go to zero since it is too packed to flow. From Figure 2 it can be seen that the expressions used by Einstein [23] and Batchelor [27] for effective viscosity do not behave in the expected manner as the proppant

reaches the saturation point, because the expressions predict a flux at high concentrations which do not account for packing of the proppant. These effective viscosity relationships are thus excluded from further study here. The relationships postulated by Eskin and Miller [28], Eilers [29], and Krieger and Dougherty [30] incorporate the expected behaviours in the limit and will be further studied.

Table 1: Effective viscosity, $\mu(\phi)$

Expression		Source
$\mu(\phi) = \mu_0(1 + B\phi)$	$B = 2.5$ [1]	Einstein (1906) [23]
$\mu(\phi) = \mu_0\left(1 + B\phi + B_1\phi^2 + ...\right)$	$B_1 = 7.6$ [2]	Batchelor (1977) [27]
$\mu(\phi) = \mu_0\left(1 + B\phi + B_1\phi^2 + B_2\exp(B_3\phi)\right)$	$B_1 = 10$ $B_2 = 0.0019$ $B_3 = 20$	Eskin and Miller (2008) [28]
	$B_1 = 10.05$ $B_2 = 0.00273$ $B_3 = 16.6$	Thomas (1965) [31]
$\mu(\phi) = \mu_0\left(1 - \frac{\phi}{\phi_m}\right)^{-\beta}$	$\beta = 2.5\phi_m$ [3]	Krieger and Dougherty (1959) [30]
	$\beta = 2.5$	Nicodemo et. al. (1974) [32]
	$\beta = 2$	Maron and Pierce (1956) [33]
	$\beta = 1.5$	Barree and Conway (1994) [34]
	$\beta = 1.82$	Krieger (1972) [35]
	$\beta = 1.89$	Scott (1984) [36]
$\mu(\phi) = \mu_0\left[1 + \left(\frac{1.25\phi}{1 - \phi/\phi_m}\right)\right]^2$		Eilers (1941) [29]

[1] Also been used with $1.5 \leq B \leq 5$ [26]
[2] Also been used with $7.35 \leq B_1 \leq 14.1$ [26]
[3] Also been used with $1 \leq \beta \leq 3$ [2]

2.4. Initial and Boundary Conditions

The conditions required to solve the proppant transport problem are described in this section. A hyperbolic problem requires initial conditions, defining the proppant concentration in the fracture at the start of the simulation by ϕ_0,

$$\phi(x, 0) = \phi_0(x), \quad \phi_0 \in C^{-1} \tag{9}$$

At the fracture tip, proppant is prevented from exiting the fracture by applying a solid wall boundary condition which restricts proppant flow,

$$q(x_{tip}, t) = 0 \tag{10}$$

Based on physical limitations, the proppant concentration is constrained to non-negative values less than or equal to the saturation concentration,

$$0 \leq \phi \leq \phi_m \tag{11}$$

Numerical methods don't constrain the solution from exceeding the physically admissible limits, so an additional algorithm is implemented in Section 3.6 to explicitly constrain the problem.

Finally, proppant bridging, or arching, occurs when particles become confined between the fracture faces at very small fracture widths. The threshold fracture width at which the particles form a bridge is a

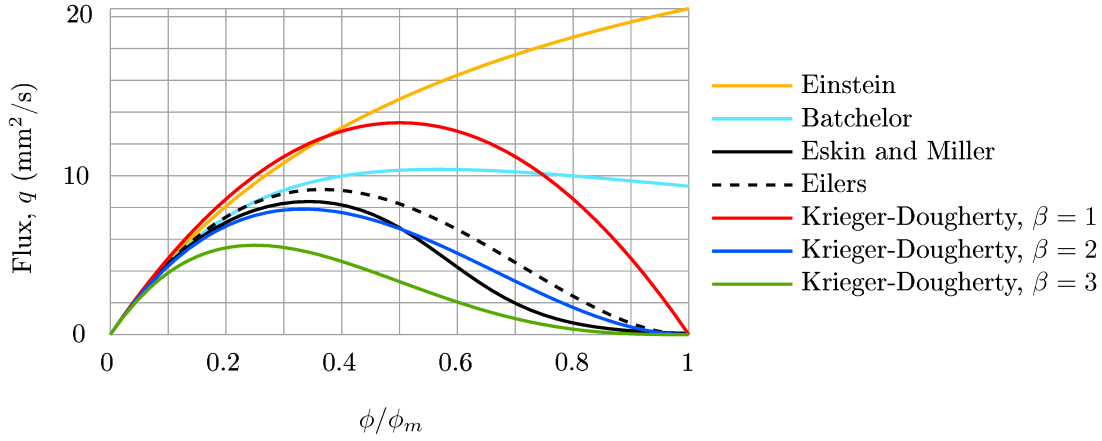

Figure 2: Proppant flux, q, for a range of normalized proppant concentrations with w=1 mm, $\partial p/\partial x$=-1 kPa/m, $\phi_m = 0.64$, and $\mu_0 = 1mPa \cdot s$

function of the average proppant diameter [37]. In this work, the proppant is restricted from flowing through a fracture width smaller than 3 proppant diameters in size. This is expressed in the formulation as

$$q(x,t) = 0 \quad \text{if } w < 3 \cdot (2a) \tag{12}$$

in which a is the average proppant radius.

3. Finite volume discretization

The finite volume method used to solve the governing equation is described in detail in this section. The one-dimensional fracture is discretized into N evenly-spaced cells of length Δx, as depicted in Figure 3. A node is placed at the center of each cell, each associated with an unknown nodal value of proppant concentration, ϕ_i, and known values of fracture width, w_i, and fluid pressure, p_i.

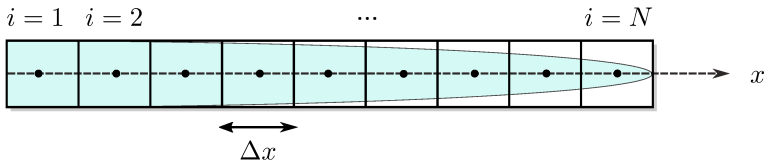

Figure 3: Finite Volume Mesh

The governing equation (7) is integrated over a single cell associated with node i over a time step (Δt) from time t_n to t_{n+1},

$$\int_{t_n}^{t_{n+1}} \int_{x_{i-1/2}}^{x_{i+1/2}} \frac{\partial(\phi w)}{dt} dx dt + \int_{t_n}^{t_{n+1}} \int_{x_{i-1/2}}^{x_{i+1/2}} \frac{\partial q}{\partial x} dx dt = 0 \tag{13}$$

in which $x_{i\pm1/2}$ denote the edges of cell i. The source term due to injection is neglected in the formulation and added later as a boundary condition. In the remainder of the text, the superscript n denotes a variable evaluated at the current time t_n, and the subscript i denotes the variable evaluated at the position x_i, i.e.,

the proppant concentration at position x_i along the fracture and time t_n is $\phi_i^n = \phi(x_i, t_n)$. The volumetric proppant flux at location x_i and time t_n is denoted by $q_i^n = q(\phi_i^n, \mu(\phi_i^n), w_i^n, p_{,xi}^n)$. Using the fundamental theorem of calculus the differential terms are eliminated from the integral equation,

$$\int_{x_{i-1/2}}^{x_{i+1/2}} \left[(\phi w)^{n+1} - (\phi w)^n\right] dx + \int_{t_n}^{t_{n+1}} \left[q_{i+1/2} - q_{i-1/2}\right] dt = 0 \tag{14}$$

Using the midpoint numerical integration rule for the first term and adopting explicit time integration (forward Euler), the discrete equation is obtained,

$$\left[(\phi w)_i^{n+1} - (\phi w)_i^n\right] \Delta x + \left[q_{i+1/2}^n - q_{i-1/2}^n\right] \Delta t = 0 \tag{15}$$

Rearranging, the standard form for the explicit finite volume formulation is obtained,

$$(\phi w)_i^{n+1} = (\phi w)_i^n - \frac{\Delta t}{\Delta x}\left[q_{i+1/2}^n - q_{i-1/2}^n\right] \tag{16}$$

The finite volume method is conservative along the cell edges since any flux leaving or entering a cell leads to a flux entering or leaving a neighbour cell. This means the total mass in the domain is preserved and only changes due to fluxes at the boundaries. The difficulty in the finite volume method is in approximating the proppant flux terms at the cell edges, $q_{i\pm1/2}^n$.

The rest of this section describes the numerical methodology used to approximate the proppant flux at the cell edges. First, the characteristic speed of proppant is defined at the cell edges. Then, the characteristic speed is used to derive an estimate of the critical time step for proppant transport problems. The types of shock waves encountered in the solution of the nonlinear advection problem are described to define the scenarios that must be addressed in the approximation of the proppant fluxes, $q_{i\pm1/2}^n$. Finally, the high-resolution proppant flux approximation (a combination of the Godunov method and Lax-Wendroff method) at the cell edges is described.

3.1. Characteristic speed of proppant

The solution to the nonlinear advection equation is dependent on the characteristic speed of the proppant, which is the speed, s, at which a constant proppant concentration profile travels through the domain,

$$s = \frac{\partial q}{\partial(\phi w)} = \frac{\partial}{\partial(\phi w)}\left(-\phi \frac{w^3}{12\mu(\phi)} \frac{\partial p}{\partial x}\right) \tag{17}$$

The proppant characteristic speed, s, for various functions of effective viscosity is plotted over the range of normalized proppant concentrations in Figure 4 for a fracture width of 1 mm, a pressure gradient of -1 kPa/m, a fluid viscosity of 1 mPa·s and a maximum proppant concentration of 0.64. These curves are all characterized by being greater than zero for low proppant concentrations, signifying that proppant travels in the direction of slurry flow. The characteristic speed crosses into the negative range between $0.2\phi_m - 0.5\phi_m$.

The proppant characteristic speed should not be confused with the direction of slurry flow. For a nonlinear advection problem, the solution remains constant along the characteristic curve, which has a slope defined by the characteristic speed. For typical fracture conditions with a negative pressure gradient inside the fracture, the proppant flux is always positive (heading towards the tip of the fracture), as shown in Figure 2. However, the characteristic speed is negative for higher proppant concentrations, as shown in Figure 4. Although the slurry is moving towards the tip of the fracture, a negative characteristic speed signifies that the net amount of proppant carried forward is limited so that the concentration builds up in the direction opposite to the flow. The curves in Figure 2 show that the characteristic speed of the nonlinear flux functions naturally captures the reversal of proppant build-up direction as the concentration increases. The sudden change in direction of characteristic speed is the cause of shock waves in the solution for a nonlinear advection problem. The concentration at which the characteristic speed changes sign is called

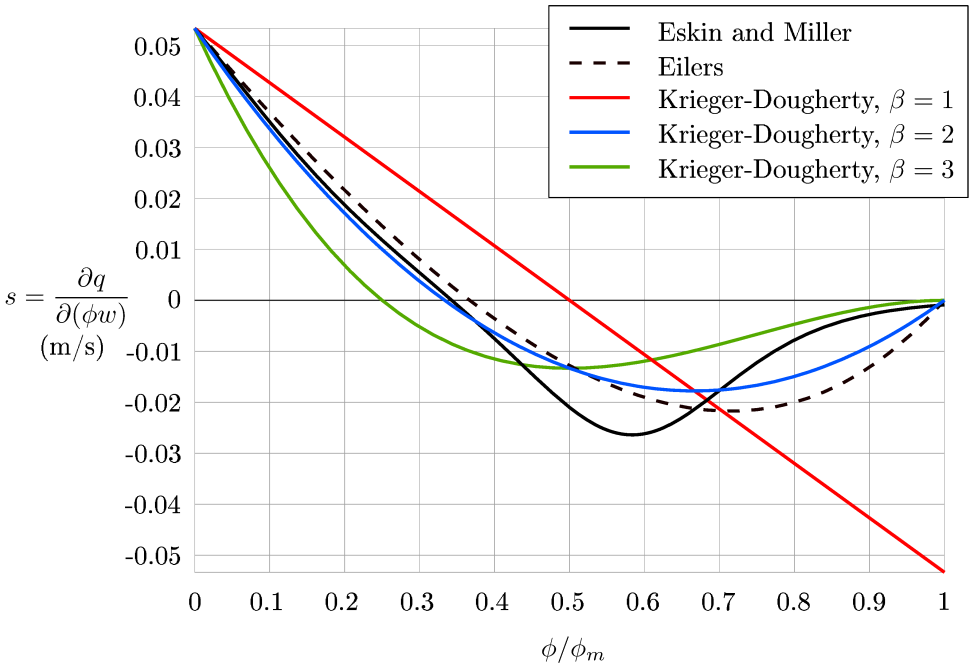

Figure 4: Approximate characteristic speed for a constant fracture width (1 mm), pressure gradient (-1 kPa/m), and fluid viscosity (1 mPa·s)

the stagnation point (or sonic point) [38], and it is shown in later sections that it is important to define the stagnation point to locate the origin of a shock wave. The stagnation point, ϕ_s, for different effective viscosity functions is provided in Table 2.

Table 2: Stagnation point for different effective viscosity functions, independent of width, w, and pressure gradient, $p_{,x}$

Effective viscosity function	Stagnation point, ϕ_s
Eskin and Miller	0.22
Eilers	$0.37\phi_m$
Krieger-Dougherty, $\beta = 1$	$0.50\phi_m$
Krieger-Dougherty, $\beta = 2$	$0.33\phi_m$
Krieger-Dougherty, $\beta = 3$	$0.25\phi_m$

The approximation of the proppant flux at the cell edges depends on the value of the proppant characteristic speed at the cell edges, denoted by $s^n_{i\pm1/2}$. Due to the complexity of the proppant flux function, an explicit expression for the characteristic speed (17) is difficult to obtain, so an approximation is used. The proppant characteristic speed is approximated as the shock speed using the Rankine-Hugoniot jump condition, or as the approximate characteristic speed at the cell center if there is no jump in the solution,

$$s_{i+1/2} = \begin{cases} \dfrac{q_{i+1} - q_i}{(\phi w)_{i+1} - (\phi w)_i}, & |(\phi w)_{i+1} - (\phi w)_i| > \varepsilon_s |(\phi w)_i| \\ \dfrac{1}{w_i} \dfrac{\partial q}{\partial \phi}\Big|_{x_i}, & |(\phi w)_{i+1} - (\phi w)_i| \leq \varepsilon_s |(\phi w)_i| \end{cases} \tag{18}$$

$$s_{i-1/2} = \begin{cases} \dfrac{q_i - q_{i-1}}{(\phi w)_i - (\phi w)_{i-1}}, & |(\phi w)_i - (\phi w)_{i-1}| > \varepsilon_s |(\phi w)_i| \\ \dfrac{1}{w_i} \dfrac{\partial q}{\partial \phi}\Big|_{x_i}, & |(\phi w)_i - (\phi w)_{i-1}| \leq \varepsilon_s |(\phi w)_i| \end{cases} \tag{19}$$

The variable ε_s is a small value used to determine whether the jump in ϕw is approaching zero and taken as 0.5 for problems in this paper. This value is surprisingly large, but smaller values were found to create oscillations in the solution for proppant transport problems.

3.2. Critical time step for proppant transport

The stable time step size for the explicit equation is limited according to the Courant-Friedrichs-Lewy (CFL) stability condition,

$$\Delta t \leq \frac{\Delta x}{s^n_{max}} \tag{20}$$

in which s^n_{max} is the maximum characteristic speed present throughout the domain at time t_n. An explicit expression for the characteristic speed is difficult to obtain for the nonlinear proppant flux since the term being advected is (ϕw). Hence, using the assumption that the fracture width is constant in the time step, it is approximated as

$$\begin{aligned} s^n_{max} &= \max\left(\frac{\partial q(\phi, w)}{\partial (\phi w)}\right) \\ &\approx \max\left(\frac{1}{w}\frac{\partial q(\phi, w)}{\partial \phi}\right) \quad , 0 \leq \phi \leq 1 \end{aligned} \tag{21}$$

It is interesting to note that the maximum characteristic speed of the proppant occurs at zero concentration for all the effective viscosity relationships shown in Figure 2. Therefore, the critical time step is the same for any selected function of effective viscosity, so long as the concentration is zero somewhere in the domain. A conservative estimate of the time step may be calculated using the proppant flux at zero concentration irrespective of the effective viscosity relationship chosen.

$$s^n_{max} \approx \max\left(\frac{-{w^n_i}^2}{12\mu_0}\frac{\partial p^n_i}{\partial x}\right), \forall i \in [0, N] \tag{22}$$

3.3. Shock waves in proppant transport problems

The sources of numerical complexity of nonlinear advection problems are the shocks that appear in the solution. The solution becomes non-smooth, and the jumps in the proppant concentration propagate throughout the domain. The jumps in proppant concentration must be properly taken into account when approximating the flux at the cell edges. This section discusses the types of shock waves that arise in the propagation of proppant, and the approximation of edge fluxes is described in detail in Section 3.4. There are four types of shocks to account for when approximating the proppant flux at cell edges:

1. the proppant concentration jumps from cell edge to cell edge because the approximate solution obtained using the finite volume method is assumed to be constant throughout the cell (discontinuities propagate from the cell edges, due to the discontinuous nature of the solution);

2. the proppant concentration builds up in one location and the build-up creates a shock that travels through the fracture (discontinuities due to characteristic curves merging between the cell centers creating a compression wave);
3. the proppant concentration disperses from an area of high concentration into parts of the fracture with low concentration (discontinuities due to characteristic curves diverging between the cell centers creating a rarefaction wave); and
4. the width or pressure gradient changes along the fracture, causing the proppant concentration to change suddenly (discontinuities due to jump in characteristic speed at cell edges).

The first type of shock that is created in the solution is a byproduct of the piecewise constant approximation of ϕ used in the finite volume method. The proppant concentration is only approximated at the center of each cell, representing the average concentration throughout the cell. At each cell edge, there is a jump in the solution which creates a jump in the characteristic speed, or the speed at which the proppant is transported through the fracture. Considering the case where the concentrations in adjacent cells are either both above the stagnation point, ϕ_s, or both below the stagnation point, the jump in the solution for proppant concentration can lead to the creation of either left-travelling or right-travelling shock waves. The creation of these shock waves is depicted in Figure 5, where the jump in proppant concentration at cell edges and the corresponding characteristic curves are shown for left- and right-travelling waves in Figures 5a and 5b, respectively. The top half of each figure depicts the portion of the fracture width filled with proppant (ϕw) for two adjacent finite volume cells, with the proppant concentration at the cell center shown in red and the cell edge represented by a dotted line. The bottom half of the figures shows the idealized characteristic curves for the proppant in each of the cells. The characteristic curve represents the curve in time and space along which the solution is constant, with the slope of the curve representing the proppant characteristic speed, s. In both scenarios shown in Figures 5a and 5b, the characteristic speed on either side of the cell edge is travelling in the same direction. The resulting shock wave has a magnitude defined by the Rankine-Hugoniot jump condition as given in Equations 18-19.

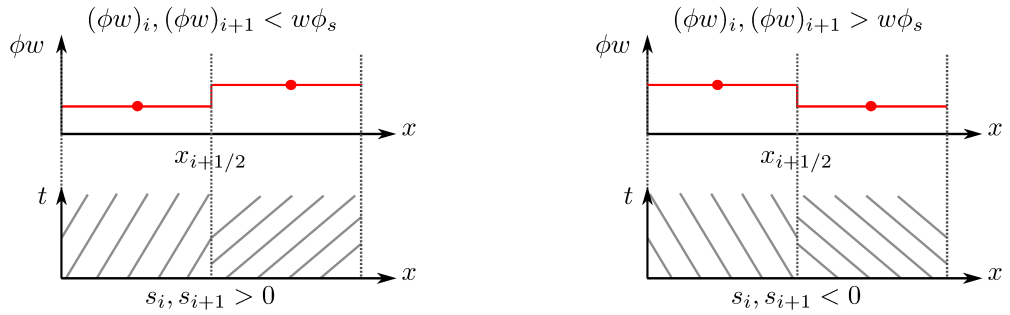

(a) Right-traveling shock wave propagating from the cell edge due to the discontinuous nature of the solution

(b) Left-traveling shock wave propagating from the cell edge due to the discontinuous nature of the solution

Figure 5: Visualization of characteristic curves during formation of shock waves propagating due to discontinuity in solution at cell edge

The second type of shock wave occurs when the proppant in each adjacent cell is travelling towards the same edge and builds up. In HF simulations, this type of shock wave occurs during the formation and growth of a plug. The accumulation of proppant concentration creates a shock wave that travels through the domain. This discontinuity stems from merging of characteristic curves within a cell, as depicted in Figure 6a, creating a compression wave. The characteristic speed is positive in the left cell, and negative in the right cell, with the solution in each adjacent cell lying on either side of the stagnation point. The resulting shock wave is naturally captured by approximating the characteristic speed using the Rankine-Hugoniot jump condition.

The third type of shock wave is generated when a build-up of proppant disperses into areas of low proppant concentration, as occurs when a proppant plug is flushed. In this scenario, the characteristic curves diverge within a cell, as depicted in Figure 6b. A rarefaction wave is created that spreads partially to the left and partially to the right of the cell edge. Similar to the compression wave, the solution in each adjacent cell is on either side of the stagnation point but located such that the proppant is travelling away from the cell edge instead of towards it. The characteristic speed is approximated using the Rankine-Hugoniot jump condition, but the magnitude of the shock wave is equivalent to the concentration at the stagnation point, given in Table 2. Therefore, the proppant flux transmitted at the cell edge is the flux corresponding to the concentration at the stagnation point, $q_s = q(\phi_s)$. The implementation is modified for the special case of a rarefaction wave and described in further detail in Section 3.4.1.

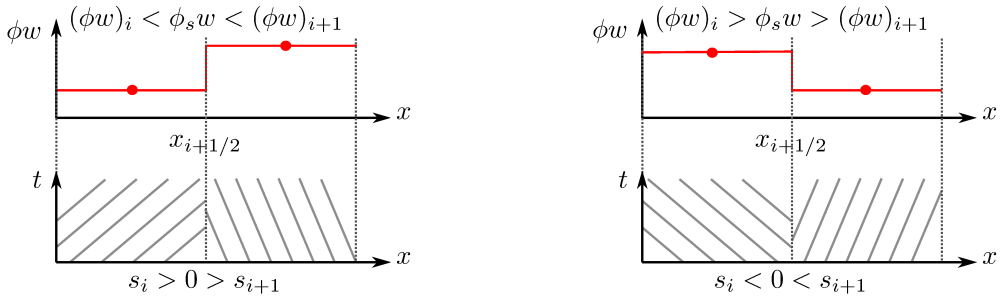

(a) Compression wave due to characteristic curves merging between the cell centers

(b) Rarefaction wave due to characteristic curves diverging between the cell centers

Figure 6: Visualization of characteristic curves during formation of compression and rarefaction waves

Finally, the fourth type of shock wave encountered is due to a change in fracture width or pressure gradient of the slurry along the fracture, as occurs due to HF propagation. Similar to the proppant concentration, both the fracture width and pressure gradient are specified at cell centers and are discontinuous at the cell edges, causing a jump in the characteristic speed at the cell edge. The jump in characteristic speed related to this spatially-varying flux function results in a stationary shock wave–an abrupt change in the solution that does not travel through the domain. The magnitude of the jump in solution is difficult to approximate, but since the flux must be conserved at the cell edge, writing the approximation in terms of the change in flux allows for the stationary shock wave to be accounted for. The implementation presented by Bale et. al. [39] is used and described in further detail in Section 3.4.2.

3.4. Approximation of proppant fluxes

The difficulty in the finite volume method is in approximating the flux terms at the cell edges, $q^n_{i\pm1/2}$. The flux is dependent on terms that are known only at the cell centers. The method selected for the approximation must take into account that the flux function is nonlinear and spatially varying, which introduces discontinuities in the solution that travel as shock waves through the domain. In this section, a high-resolution method is described which accounts for the shock waves described in the previous section. On their own, the Godunov method and the Lax-Wendroff method add numerical inaccuracies to the solution [38]. The Godunov method adds numerical diffusion (over-smoothing) and the Lax-Wendroff method adds numerical dispersion (lag). The best features of the two methods are maintained by using a high-resolution method that combines them using Total Variation Diminishing (TVD) slope limiters. These methods are described in detail in the following sub-sections. Using an explicit formulation, all values are computed at the current time, t_n. For simplicity, all superscripts n are excluded in this section, but it is implied that all values are calculated at the current time step.

3.4.1. Godunov method

The Godunov method approximates the flux at the cell edges, $q_{i\pm1/2}$, by solving the Riemann problem at each of these edges using the characteristics. This method provides a first-order approximation which naturally accounts for discontinuities propagating left and right, and characteristics merging between the cell centers (shock waves of type 1 and 2 mentioned in the previous section). In the case of a linear flux function, $q = c\phi$ with constant-valued c, the Godunov method is identical to the first-order upwinding method.

A rarefaction wave where proppant spreads between the cell centers as depicted in Figure 6b is not captured naturally using the Godunov method. The Godunov method may lead to an incorrect solution which does not satisfy the so-called entropy condition [38], a term that comes from gas dynamics but is applicable to other nonlinear advection problems. In terms of proppant transport, the physical interpretation of the entropy condition is that the total proppant mass must be conserved within the domain. To ensure that the entropy condition is satisfied, the flux that is propagated in the rarefaction wave is equal to the flux at the stagnation point, $q_s = q(\phi_s)$. The stagnation points are given in Table 2 for various expressions of viscosity. To correctly capture the rarefaction wave, the Godunov method with an entropy fix approximates the flux at the cell edges as,

$$q^G_{i+1/2} = \begin{cases} q_s, & s_{i+1} > 0 \text{ and } s_i < 0 \\ q_i, & s_{i+1/2} \geq 0 \\ q_{i+1}, & s_{i+1/2} < 0 \end{cases} \tag{23}$$

$$q^G_{i-1/2} = \begin{cases} q_s, & s_i > 0 \text{ and } s_{i-1} < 0 \\ q_{i-1}, & s_{i-1/2} \geq 0 \\ q_i, & s_{i-1/2} < 0 \end{cases} \tag{24}$$

The formulation is based on the flux at cell centers, q_i, for $i = 1, 2, ..., N$. If there is no rarefaction wave, the selection of the flux is based on the direction of the characteristic speed at the cell edges, $s_{i\pm1/2}$, computed by Equations 18-19.

The rarefaction wave is characterized by a proppant concentration on either side of the stagnation point. The flux functions of interest in proppant transport have two stagnation points, as shown in Figure 4. One occurs for a normalized proppant concentration, ϕ/ϕ_m, between 0.2 and 0.5 depending on the expression of effective viscosity used, and the other occurs for a normalized proppant concentration $\phi/\phi_m = 1$. The range of physically admissible normalized proppant concentrations is between 0 and 1, so the stagnation point at a normalized proppant concentration of 1 is typically not encountered in simulations. However, this formulation is able to capture both stagnation points.

3.4.2. Lax-Wendroff method

The first-order Godunov method adds numerical diffusion to the solution, particularly near shock waves where the gradient of the concentration profile is steep. For this reason, a high-resolution method is required to avoid over-smoothing of the solution and maintain a sharp proppant front. The Lax-Wendroff method provides a second-order approximation and contains anti-diffusive terms in the formulation which cancel out the numerical diffusion created in the Godunov method [38].

The Lax-Wendroff method is typically written in terms of the jump in proppant concentration at the cell edge, $\Delta\phi$. For spatially-varying flux functions, the jumps in proppant concentration also arise because the fracture width and pressure gradient are discontinuous at cell edges. The jump in concentration at the cell edge is therefore not a straightforward calculation based on the values at the neighbouring nodes. Using the fact that flux is conserved at the cell edge, Bale et. al. [39] wrote the Lax-Wendroff approximation in terms of the change in flux, Δq, which is equipped to handle spatially-varying fluxes and does not require an explicit calculation of the change in concentration, $\Delta\phi$, at the cell edge. The approximation of flux at the cell edges using the Lax-Wendroff method based on flux waves is

$$q_{i+1/2} = \Delta q_{i+1/2} H(s_{i+1/2} < 0) + \underbrace{\frac{1}{2}\text{sign}(s_{i+1/2})\left(1 - \frac{\Delta t}{\Delta x}|s_{i+1/2}|\right)\Delta q_{i+1/2}}_{q^{LW}_{i+1/2}} \tag{25}$$

$$q_{i-1/2} = -\Delta q_{i-1/2} H(s_{i-1/2} \geq 0) + \underbrace{\frac{1}{2}\text{sign}(s_{i-1/2})\left(1 - \frac{\Delta t}{\Delta x}|s_{i-1/2}|\right)\Delta q_{i-1/2}}_{q^{LW}_{i-1/2}} \tag{26}$$

where the flux wave is defined as the change in flux at the cell edge, $\Delta q_{i+1/2} = q_{i+1} - q_i$, and $H()$ is the Heaviside step function. The first term in the approximation is equivalent to the Godunov method without the entropy fix, and the second term can be seen as a correction term for the diffusion in the Godunov method. The correction term, $q^{LW}_{i\pm1/2}$, is used in the following section to define a high-resolution method.

3.4.3. High resolution method

The Lax-Wendroff method eliminates the numerical diffusion seen in the Godunov method but adds some lag (numerical dispersion) to the solution. To take advantage of the properties of the Godunov method when the solution is smooth, and the Lax-Wendroff method when there is a sharp gradient in the solution, a flux limiter method is used. The flux approximation at the cell edges is given by

$$\begin{aligned} q_{i+1/2} &= q^{G}_{i+1/2} + \varphi(r_{i+1/2}) q^{LW}_{i+1/2} \\ q_{i-1/2} &= q^{G}_{i-1/2} + \varphi(r_{i-1/2}) q^{LW}_{i-1/2} \end{aligned} \tag{27}$$

where the superscripts G and LW refer to the Godunov approximation (23-24) and the correction term in the Lax-Wendroff approximation (25-26), respectively.

The function $\varphi(r)$ is called the limiter function, which is responsible for applying the second-order corrections when there is a sharp gradient in the solution. The limiter function varies between 0 for a smooth concentration profile and 1 for a sharp jump in concentration, effectively working to add more of the Lax-Wendroff correction near discontinuities. Various limiter functions have been developed, with the key feature of them being that they are Total Variation Diminishing (TVD). The total variation of the solution is the sum of the jump in concentration at all cell edges throughout the domain. Oscillations introduced by the numerical method would increase the total variation of the solution over time. TVD limiters functions are chosen to avoid adding oscillations by requiring that the method not increase the total variation of the solution. A review of possible limiters can be found in Leveque [38]. This work uses the monotized central-difference limiter (MC) limiter, defined as

$$\varphi(r) = \max(0, \min((1 + r)/2, 2, 2r)) \tag{28}$$

No significant difference is observed in the numerical results presented in Section 4 when compared with simulations using the Min-Mod, Superbee, and Van Leer limiters. The variable r in the limiter function is the slope ratio, which relates the upwind concentration gradient to the gradient at the cell edge,

$$r_{i+1/2} = \begin{cases} \dfrac{(\phi w)_i - (\phi w)_{i-1}}{(\phi w)_{i+1} - (\phi w)_i}, & s_{i+1/2} \geq 0 \\ \dfrac{(\phi w)_{i+2} - (\phi w)_{i+1}}{(\phi w)_{i+1} - (\phi w)_i}, & s_{i+1/2} < 0 \end{cases} \tag{29}$$

$$r_{i-1/2} = \begin{cases} \dfrac{(\phi w)_{i-1} - (\phi w)_{i-2}}{(\phi w)_i - (\phi w)_{i-1}}, & s_{i-1/2} \geq 0 \\ \dfrac{(\phi w)_{i+1} - (\phi w)_i}{(\phi w)_i - (\phi w)_{i-1}}, & s_{i-1/2} < 0 \end{cases} \tag{30}$$

To define the upwind direction, the characteristic speed at the cell edge is approximated as described in Section 3.1. The sign of the approximated characteristic speed is used to determine the upwind direction for calculation of the slope ratio.

3.5. Boundary conditions

Flux boundary conditions are applied on both sides of the domain. At the wellbore (left edge of the domain) is an inflow boundary, which is implemented by prescribing the injection flux on the left edge of the first cell,

$$q_{1/2} = \phi_{inj} q_{inj} \tag{31}$$

At the fracture tip (right edge of the domain) is a solid wall boundary, which is prescribed by setting the flux on the right edge of the last cell to zero,

$$q_{N+1/2} = 0 \tag{32}$$

3.6. Proppant concentration constraints

Since the approximation of fluxes is not perfect, it is possible to obtain non-physical concentration values, outside the range $\phi \in [0, \phi_m]$. To avoid this, the predictor-corrector algorithm described below is implemented to prevent proppant from flowing into cells that have already reached the maximum concentration, ϕ_m, and to prevent proppant from leaving cells that are at the minimum proppant concentration, $\phi = 0$. The predictor step uses the flux approximation described in the previous sub-sections to solve for the proppant concentration at the next time step. Then, the set of cells that have a concentration outside the allowable range are identified and the fluxes going in/out of those cells are adjusted so that the final concentration is exactly the limit value. Finally, the concentration at the next time step is calculated using the adjusted fluxes.

1. *Predictor step*: solve for concentration at the next time step ($\phi_{i,p}^{n+1}$) using the approximated fluxes ($q_{i+1/2}^n$ and $q_{i-1/2}^n$),

$$\phi_{i,p}^{n+1} = \phi_i^n - \frac{\Delta t}{w_i^n \Delta x} \left(q_{i+1/2}^n - q_{i-1/2}^n \right) \tag{33}$$

   (a) Identify the set of cells with concentrations which are not within the allowable range (S^+ and S^- are the sets of cells which have a proppant concentration above the maximum(ϕ_m)/below the minimum ($\phi = 0$), respectively).

   (b) Correct the fluxes according to the current inflow/outflow:

   - For cells in set S^+, the correction flux is defined as $q_{correct}^+ = w_i^n \dfrac{\Delta x}{\Delta t}(\phi_i^n - \phi_m)$.

   The corrected cell edge flux approximations, $q_{i\pm1/2}^c$, are defined depending on the predictor flux approximation, as defined in Figure 7.

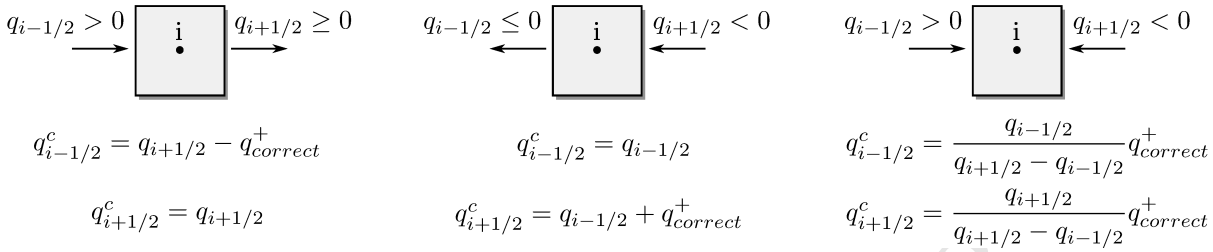

Figure 7: Corrected cell edge fluxes for cells in set S^+

- For cells in set S^-, the correction flux is defined as $q^-_{correct} = w^n_i \dfrac{\Delta x}{\Delta t} \phi^n_i$.

  The corrected cell edge flux approximations, $q^c_{i\pm1/2}$, are defined depending on the predictor flux approximation, as defined in Figure 8.

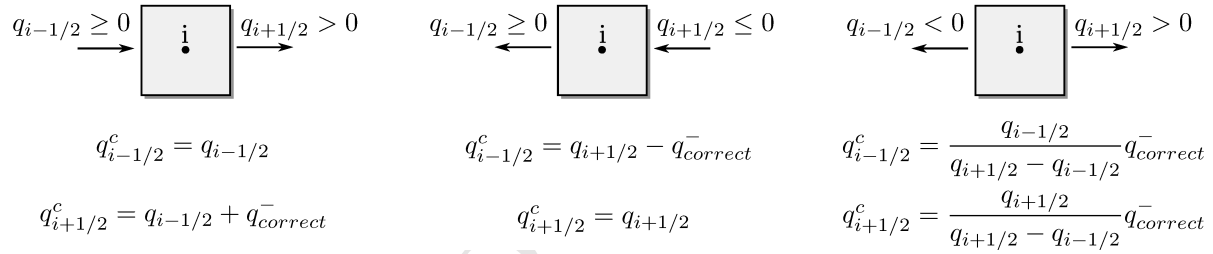

Figure 8: Corrected cell edge fluxes for cells in set S^-

(c) Update the fluxes for the neighboring cells accordingly to maintain conservation property.

2. *Corrector step*: solve for concentration using the corrected fluxes, $\phi^{n+1}_i = \phi^n_i - \dfrac{\Delta t}{w_i \Delta x} \left(q^c_{i+1/2} - q^c_{i-1/2} \right)$.
3. Set the approximation to the corrected fluxes, $q^n_{i+1/2} = q^c_{i+1/2}$, and repeat if any concentrations are still outside the acceptable range (in simulations it was found that repetitions are rarely required).

4. Numerical results

In this section, the implementation of the numerical methodology is verified for the case of a rarefaction wave and a compression wave. Proppant transport through an elliptical fracture is studied, and the limit injection rate is found for which a proppant plug occurs at the inlet. Finally, proppant flow through a plane-strain KGD fracture is investigated in which proppant bridging is observed, and the use of a concentration constraint is investigated. All results are compared using various expressions for effective viscosity. Parameters that are constant for all cases are specified in Table 3.

4.1. Injection and growth of propped fractures

The first problem considered is proppant advection in a 100 m channel of constant width (2 mm) and constant pressure gradient (-0.5 kPa/m) that is initially packed with proppant on the left half ($x < 0$) with a concentration of $0.9\phi_m$. The initial conditions prescribed, shown in Figure 9a, occur in hydraulic

Table 3: Material Properties

Parameter	Variable	Value	Unit
Maximum proppant concentration	ϕ_m	0.64	
Carrier fluid viscosity	μ_0	1.2	mPa·s
Average proppant radius	a	0.3	mm

fractures at the fracture inlet where the injected proppant builds up quickly. The proppant must spread to the surrounding fracture which does not yet contain any proppant. This concentration profile also arises in the case of a propped fracture with a saturated concentration at the tip. As such a fracture grows in length, the proppant flows into the new fracture segment that is initially void of proppant.

Solution of the nonlinear advection equation with the initial proppant concentration described results in a rarefaction wave spreading from the jump in concentration–the characteristic speed is negative to the left of the proppant front, and positive to the right of the proppant front and therefore causes concentration to diminish for $x < 0$ and increase for $x > 0$. Although a constant channel width and pressure gradient is not representative of conditions in a hydraulic fracture, the problem is used for verification of the numerical method and ensures that the rarefaction wave can be adequately captured by the entropy fix described in Section 3.4.1. This problem resembles the so-called green-light problem in traffic flow simulations, which models the advection of vehicles when a traffic light turns green [38]. In fact, the Krieger-Dougherty equation for effective viscosity of the fluid with $\beta = 1$ has the same form as the linear traffic flow equation and produces the same shape of the rarefaction curve.

The channel is discretized with 500 cells. Outflow boundary conditions are applied on both ends of the channel, allowing the proppant to leave the domain at these boundaries. There is no injection of proppant into the domain, simply advection of the initial proppant concentration for 500 seconds. The problem is solved using various forms of the flux function, and the resulting concentration profiles throughout the simulation time are shown in Figure 9. In all cases, proppant concentration is reduced to the left of the initial discontinuity ($x < 0$), and increased to the right ($x > 0$). The shape of the rarefaction wave over time is dependent on the characteristic speed of the flux function. The proppant characteristic speed corresponding to the initial proppant concentration profile is shown for each viscosity expression in Figure 10. The curve of the characteristic speed matches the curve of the corresponding rarefaction wave in Figure 9. The concentration at which the proppant front smooths out is the stagnation point, provided in Table 2. For the nonlinear characteristic speed curves that are double-valued, the equal-area rule determines the location of the shock front theoretically [38]. The theoretical curves match the resultant concentration profiles after rarefaction, verifying the shape of the solution. For the same initial proppant concentration, use of the Krieger-Dougherty equation with $\beta = 1$ leads to the most proppant spreading, while $\beta = 3$ leads to the least spreading of the proppant. The other viscosity functions lead to concentration profiles that lie between these two limits.

4.2. Plug formation and growth

The next problem considered is proppant advection in a 50 m channel of constant width (2 mm) and constant pressure gradient (-0.5 kPa/m) that is initially packed with proppant on the right half ($x > 0$) with a concentration of $0.9\phi_m$. The left half of the channel ($x < 0$) has a concentration of $0.3\phi_m$. The initial concentration profile prescribed in this problem (seen in Figure 11a) leads to a compression wave which moves towards the left of the channel, representing proppant build-up at a plug. This concentration profile may arise for a plug forming at the fracture tip, or proppant bridging along the length of the channel where the fracture width is not large enough for the proppant to flow through. This problem is used for verification of the numerical method, ensuring that the compression wave can be adequately captured using the flux approximation described in Section 2.3 and that concentration limits are not exceeded. This problem resembles the so-called red-light problem in traffic flow simulations, which models the advection of vehicles when a traffic light turns red [38].

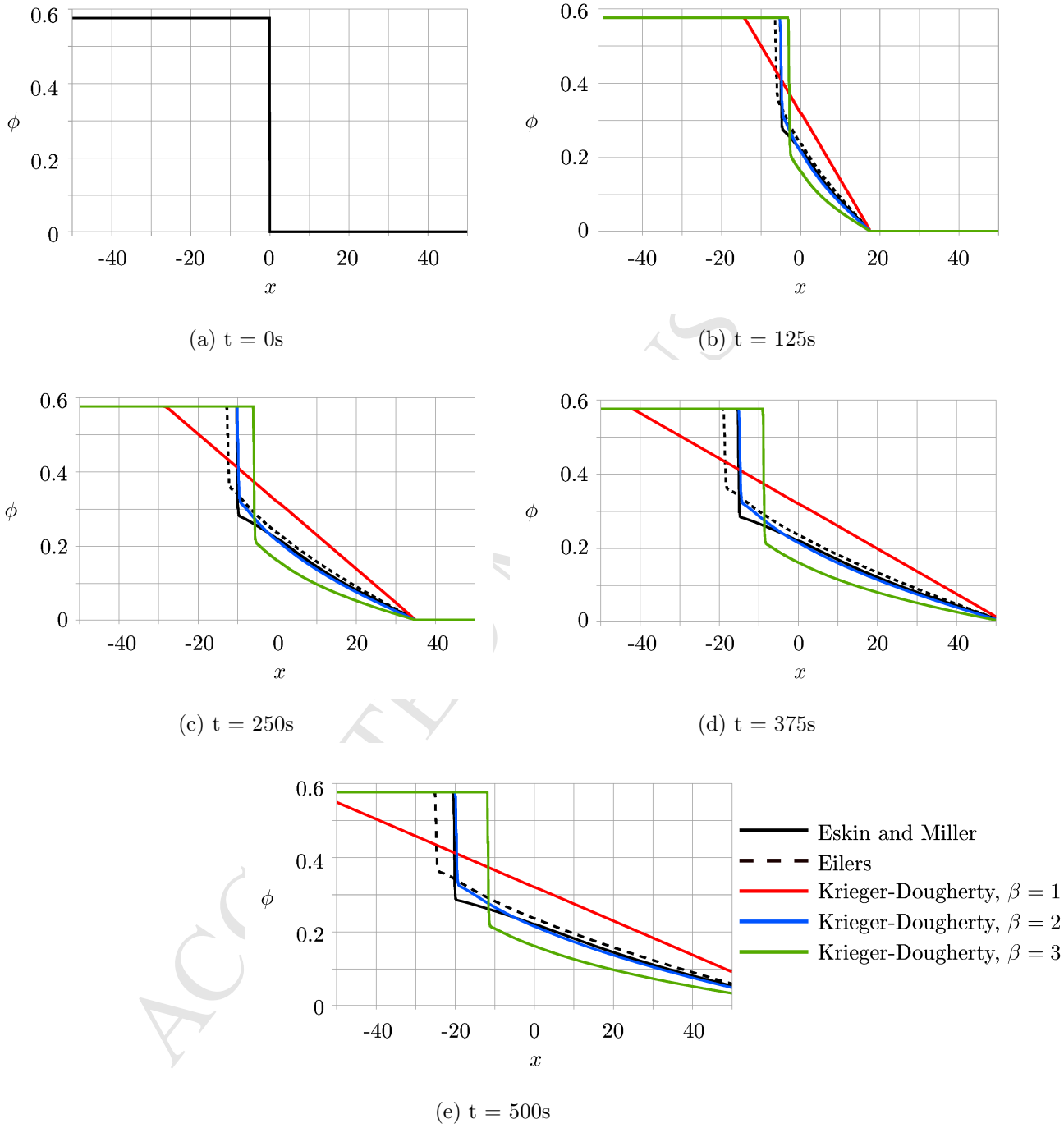

(a) t = 0s

(b) t = 125s

(c) t = 250s

(d) t = 375s

(e) t = 500s

Figure 9: Proppant concentration spreading at inlet for various times

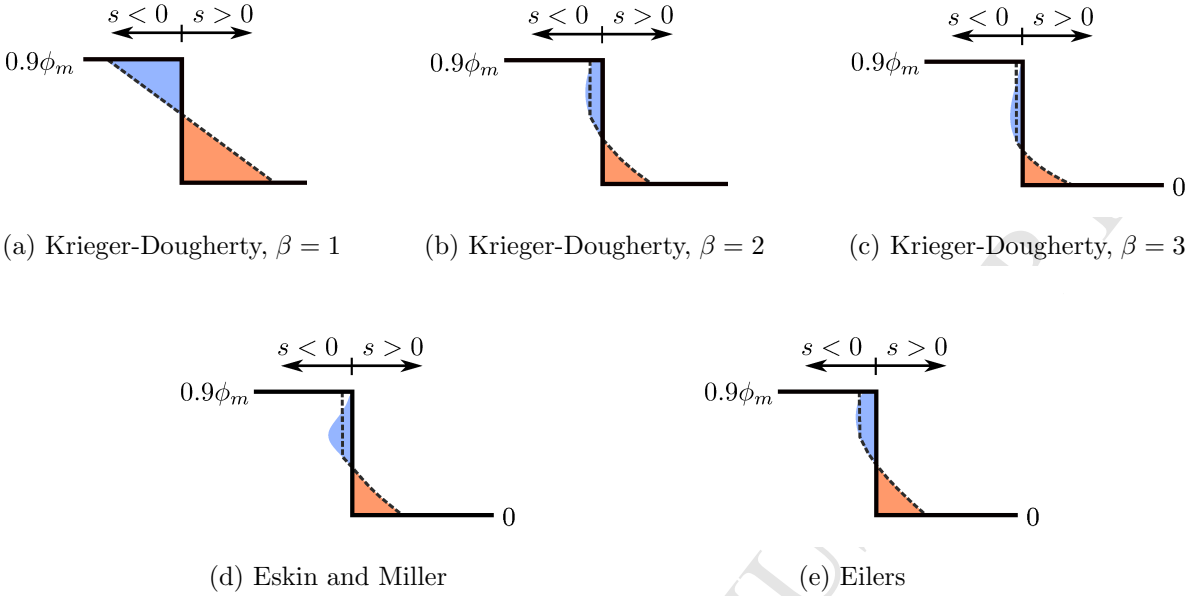

Figure 10: Theoretical characteristic speed patterns for rarefaction waves

The channel is discretized using 500 cells and advection of the initial concentration profile lasts 500 seconds. The proppant concentration throughout the simulation time is shown for various expressions of effective viscosity in Figure 11. In all the cases shown, the proppant concentration builds up to the left of the discontinuity ($x < 0$). The shape of the compression wave is also dependent on the characteristic speed, depicted for the initial concentration profile in Figure 12. The resulting concentration profiles match the theoretical curves obtained from the characteristic speed patterns, after applying the equal-area rule for multi-valued solutions [38]. Similar to the first test case in Section 4.1, use of the Krieger-Dougherty equation with $\beta = 1$ leads to the fastest-moving shock wave and $\beta = 3$ is the slowest-moving shock wave.

4.3. Inject into an elliptical fracture with constant pressure gradient

The proppant flux is a function of the proppant concentration, fracture width, and fluid pressure gradient. The verification cases performed in the previous sections had a constant fracture width and pressure gradient, with nonlinearity coming only from the proppant concentration. The next problem studies proppant advection through a 100 m long elliptical channel with a maximum fracture width of 3 mm. A constant pressure gradient of -0.5 kPa/m is maintained throughout the fracture length. Although a constant pressure gradient is not representative of conditions in a hydraulic fracture, this condition is useful for studying the shocks in the solution that originate due to nonlinearity in the fracture width.

The channel is discretized using 500 cells. The proppant width is calculated at the center of each finite volume cell and adds another spatially-varying term in the flux function. A solid wall boundary condition (32) is applied to the fracture tip on the right-hand side of the domain. Proppant is injected at a constant volumetric concentration of 0.1 for 800 seconds, with an inlet flux given in Table 4 for each viscosity expression studied.

A blocking function is included in the flux formula, which prevents proppant from flowing into a cell with a fracture width less than 3 proppant diameters in size, as defined in Equation 12. Figure 13 shows the proppant concentration profiles for various times using five different expressions for effective viscosity. The injected proppant travels towards the tip of the fracture as a rarefaction wave, with the narrowing fracture width creating a small build-up of proppant ahead of the concentration jump (see Figure 13b). Once the proppant front reaches 80m, the small fracture width causes bridging and prevents proppant from flowing to the tip, as seen in Figure 13c. The proppant builds up to the saturation concentration and another

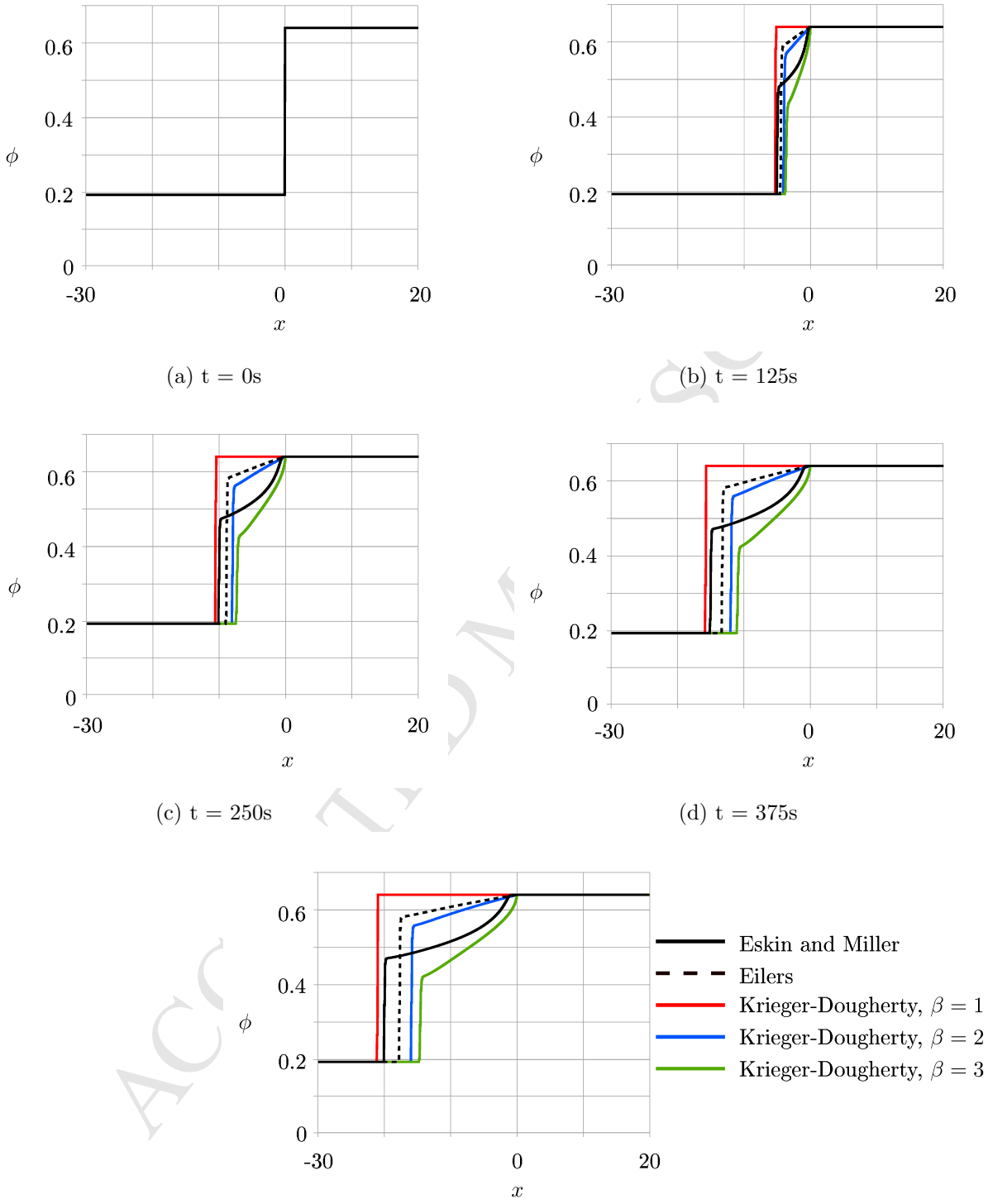

(a) t = 0s

(b) t = 125s

(c) t = 250s

(d) t = 375s

(e) t = 500s

Figure 11: Proppant concentration backing up at a plug for various times

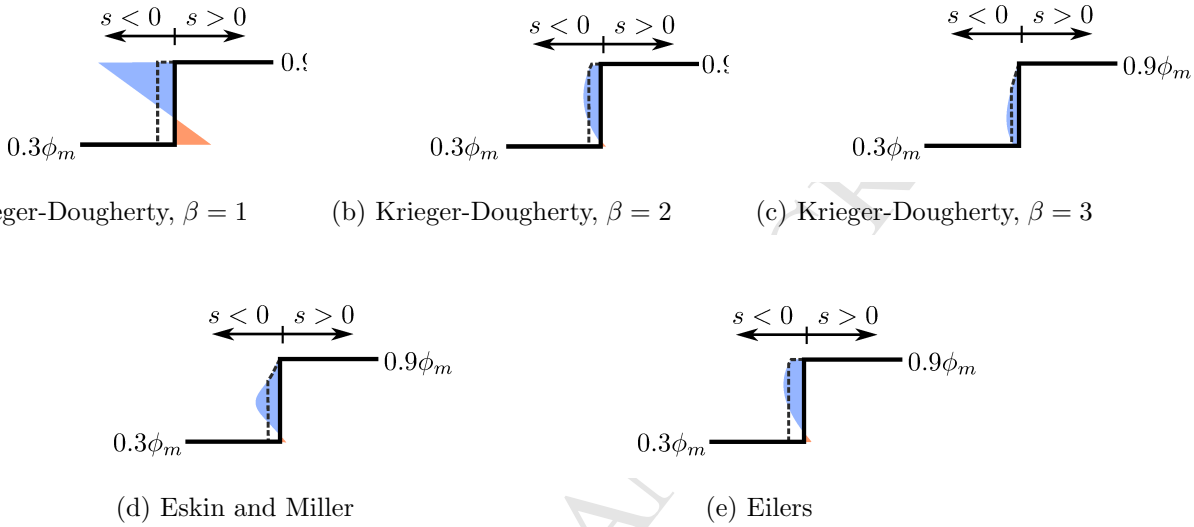

(a) Krieger-Dougherty, $\beta = 1$ (b) Krieger-Dougherty, $\beta = 2$ (c) Krieger-Dougherty, $\beta = 3$

(d) Eskin and Miller (e) Eilers

Figure 12: Theoretical characteristic speed patterns for compression waves

Table 4: Injection rate used to maintain injection concentration of $\phi_{inj} = 0.1$ for various expressions of effective viscosity

Viscosity Expression	$\phi_{inj}(t)q_{inj}(t) = 0.1\dfrac{-w^3}{12\mu(0.1)}\dfrac{\partial p}{\partial x}$
Eskin and Miller	68.730 mm^2/s
Eilers	71.117 mm^2/s
Krieger-Dougherty, $\beta = 1$	79.101 mm^2/s
Krieger-Dougherty, $\beta = 2$	66.742 mm^2/s
Krieger-Dougherty, $\beta = 3$	56.313 mm^2/s

shock wave emerges forcing the proppant to build up towards the inlet. In Figure 13d two shock fronts are visible–one moving towards the right from the initial injection spreading and one moving towards the left as the proppant plug grows from the screen-out point. Dontsov and Peirce [13] propose a modified blocking function which provides a smoother transition for the on/off status of the function. No difference was found in the solution when tested with the modified version, which shows that Dontsov's modification approximates the condition very well. The approximation using the Krieger-Dougherty equation with $\beta = 1$ creates the fastest proppant transport towards the tip and subsequent build-up, while the slowest advection occurs using $\beta = 3$.

A study of the injection rates is performed using the Krieger-Dougherty effective viscosity expression with $\beta = 3$. It is found that there is a maximum injection flux permitted before a build-up of proppant occurs at the inlet. For the material and fracture properties used in this study, the maximum injection flux is 63.281 mm^2/s, which corresponds to the flux at the stagnation point, q_s. Figure 14a shows the concentration profile after 800 seconds of injection at the maximum injection flux. The concentration at the inlet is $0.25\phi_m$, which corresponds to the concentration at which the maximum proppant flux occurs (see Figure 2), and is equivalent to the stagnation point shown (i.e., $\phi_s = 0.25\phi_m$). The stagnation point, ϕ_s, thus defines the maximum injection rate. Any flux smaller than the maximum leads to a lower concentration at the inlet, but ultimately the same concentration profile at the plug, as shown in Figure 14b. An injection flux exceeding the maximum injection flux will result in a build-up of proppant at the inlet, as shown in Figure 14c. However, the proppant still enters the fracture and the concentration profile at the plug is the same as the other cases.

The maximum injection flux is dependent on the expression for effective viscosity and is lower than injection rates reported in the literature [1]. In reality, as the injection rate increases the increased pressure at the inlet will also cause a change in the fracture width that prevents plugging at the tip. A coupled solution with the solid deformation of the rock is required to capture all the physics, but the interesting point learned from this study is that the build-up of proppant causing a plug at the inlet can be determined by the flux function using the appropriate effective viscosity function.

4.4. Injection into KGD fracture

Proppant advection through a hydraulic fracture is simulated by discretizing the fracture into 500 finite volume cells. The approximate solution for a finite, plane-strain fracture (KGD) derived by Dontsov [40] was used to obtain the fracture width and pressure along the fracture length after injecting pad fluid for 30 min at a rate of 0.01 m^3/s into a 10 m high fracture. The solution is obtained for a rock mass with Young's modulus of 40 GPa, Poisson's ratio of 0.25, fracture toughness of 1 MPa$\sqrt{m}$, and Carter leak-off coefficient of 0.001 m/min. The fracture propagates to 213.1 metres in 30 min, with a width and pressure gradient profile as shown in Figure 15. The pressure gradient is calculated using a forward difference from the pressure profile. Due to the blocking function, proppant only flows through the portion of the fracture that has a width less than 3 proppant diameters in size and the proppant does not reach the fracture tip. The pressure gradient throughout the majority of the fracture length is approximately -500 Pa/m, with a much higher pressure gradient at the inlet of 25 kPa/m, and at the fracture tip. An accurate pressure profile for a hydraulic fracture can only be obtained through a fully coupled model since the proppant concentration will change the effective viscosity of the fluid and increase the fluid pressure. This problem is used to demonstrate the types of shocks that occur in the proppant transport solution due to the large changes in pressure gradient at the fracture inlet.

Maintaining a constant width and pressure profile, proppant slurry is injected into the fracture for 30 min at a rate of 40 mm^2/s. The concentration profiles for various times throughout the injection are shown in Figure 16 for several effective viscosity expressions. The advection is affected by both the nonlinear fracture width and the nonlinear pressure gradient along the length of the fracture. The steep change in pressure gradient at the inlet causes the proppant to build-up around 50 m into the fracture as it spreads towards the fracture tip. Proppant bridging occurs approximately 150 m into the fracture at which point the concentration reaches the saturation point and builds up towards the inlet. The Krieger-Dougherty viscosity function with $\beta = 1$ results in the fastest proppant transport towards the fracture tip and also the fastest build-up at the tip. In contrast, the function with $\beta = 3$ produces the most build-up of proppant

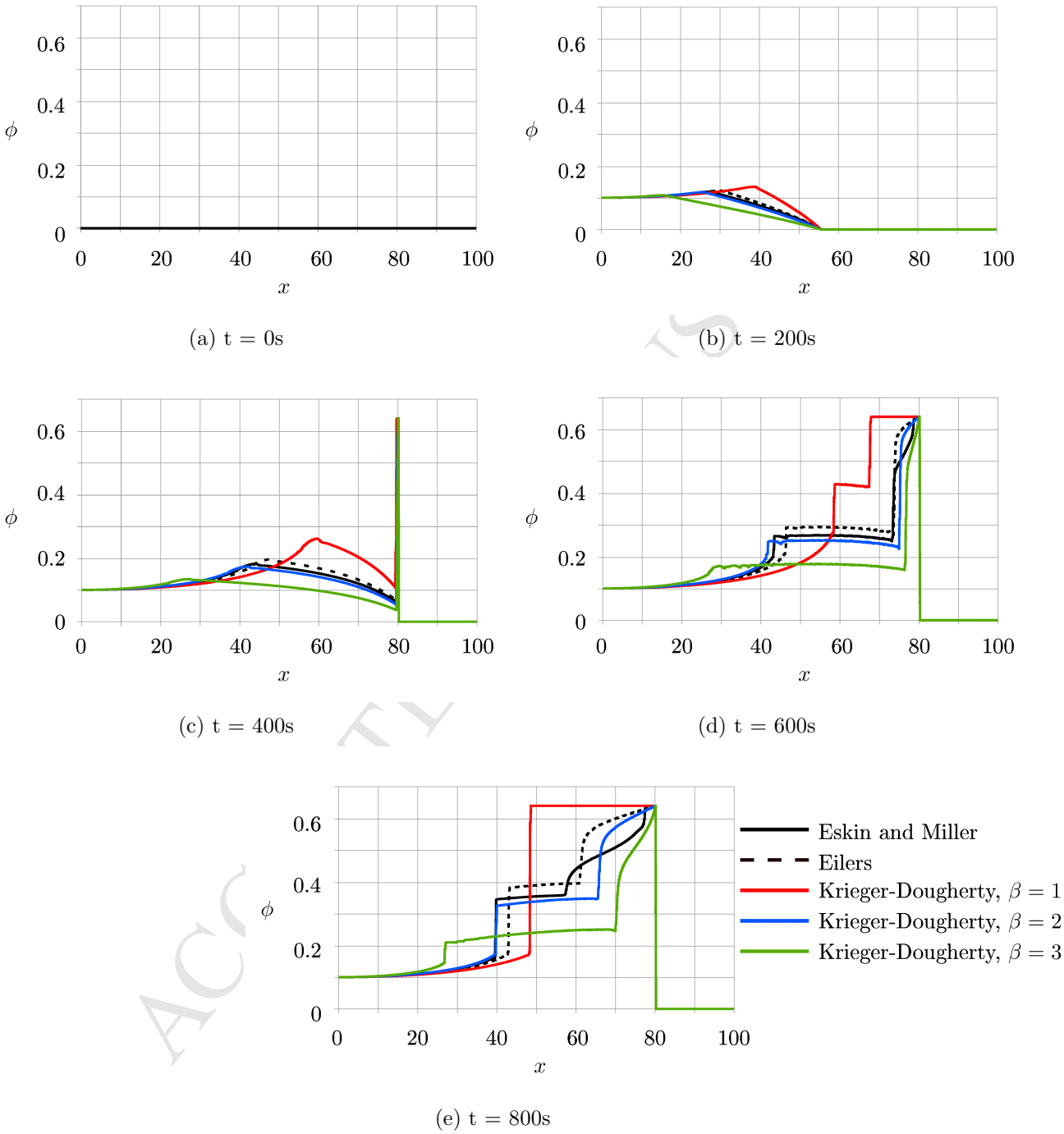

(a) t = 0s

(b) t = 200s

(c) t = 400s

(d) t = 600s

(e) t = 800s

Figure 13: Proppant injection into an elliptical fracture with constant pressure gradient, for various times

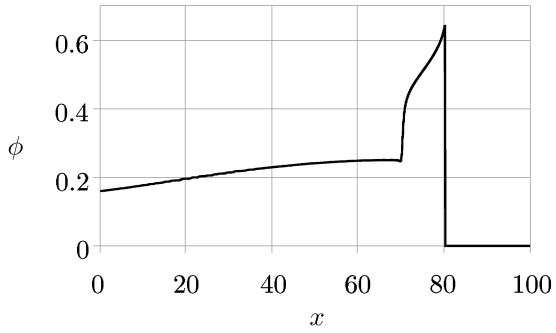

(a) Maximum injection flux = 63.3 mm^2/s

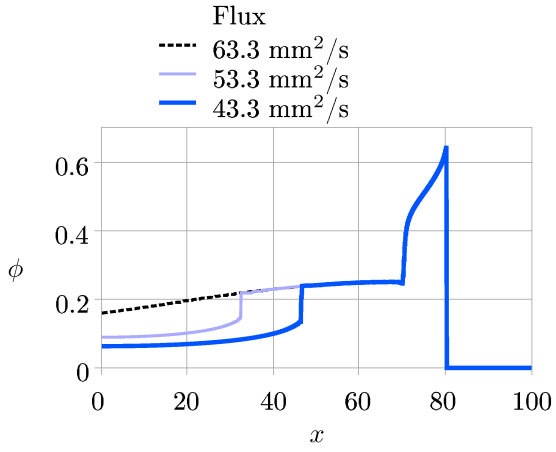

(b) Injection flux less than maximum

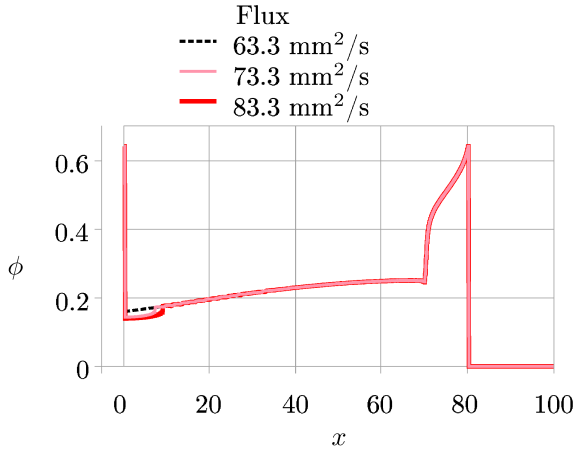

(c) Injection flux greater than maximum

Figure 14: Proppant injection into an elliptical fracture with constant pressure gradient, at t = 800s, for various injection rates

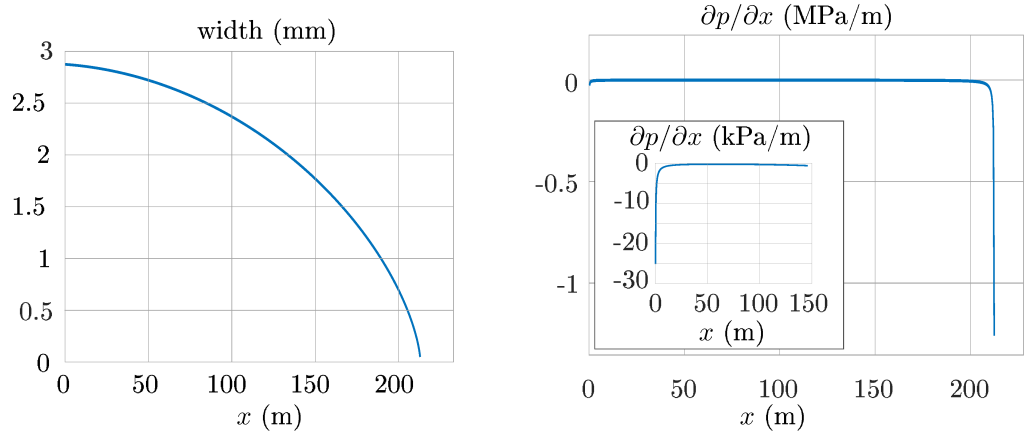

(a) Width profile for KGD fracture [40]

(b) Pressure gradient profile for KGD fracture [40]

Figure 15: Width and pressure along the fracture length

near the inlet and slowest build-up at the plug. These two viscosity functions represent the limits for all problems studied in this paper.

Implementation of the concentration constraint described in Section 3.6 makes the solution stable and remain within the physical bounds. It is most common to see the concentration exceed the maximum either near the boundary or at a tip-screen out location. In unrefined meshes, oscillations due to a poor approximation may cause the concentration to exceed the maximum as well. In these situations, the concentration constraint prevents the problem from becoming unbounded. The concentration profiles obtained without imposing the constraint are shown in Figure 17 (dashed lines). In some cases, the solution oscillates above the limit, as in Figure 17a. In other cases, the solution becomes unbounded and the last cell increases in concentration without allowing a build-up of proppant in neighbouring cells, such as in Figures 17b and 17e. These non-physical concentrations are avoided by imposing concentration constraints.

5. Conclusion

The numerical methodology for solving the nonlinear hyperbolic partial differential equation that describes proppant transport through a hydraulic fracture is presented in this paper. Many of the HF models to date solve the coupled equations governing rock deformation and fluid flow, and then loosely couple the linearized proppant transport equation at the end of each time step. The advection equation is typically linearized by assuming a constant fluid velocity. The work presented focuses solely on the solution of the proppant transport equation, without assuming a linear form for the proppant flux function. Instead, a nonlinear advection problem is solved in which a constant pressure gradient is assumed rather than a constant flow velocity.

The finite volume method using the Godunov approximation with an entropy fix and a high-resolution correction using slope limiters is used. This methodology is capable of capturing the shock waves in the solution which arise from the spatially-varying fracture width and fluid pressure gradient along the fracture (especially at the fracture tips and inlet), as well as the rarefaction wave that emerges when a proppant build-up disperses into a fracture. A predictor-corrector algorithm is proposed for constraining the concentration within physically allowable limits. Additionally, proppant bridging is simulated by limiting the proppant flux for fracture widths less than a threshold size. A critical time step is derived for proppant transport problems which works for any effective viscosity function used to describe the slurry.

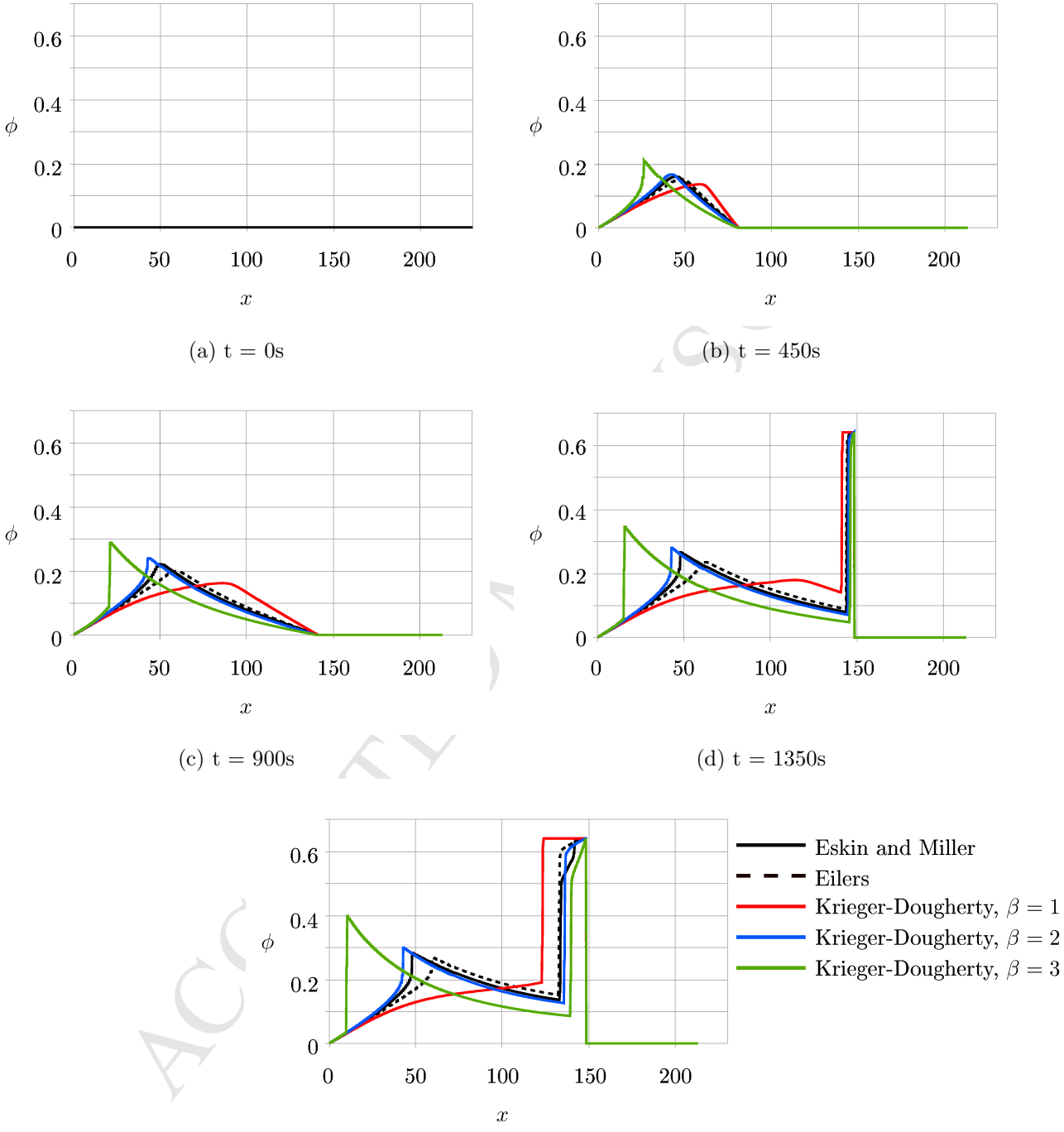

(a) t = 0s

(b) t = 450s

(c) t = 900s

(d) t = 1350s

(e) t = 1800s

Figure 16: Proppant injection into a KGD fracture, for various times

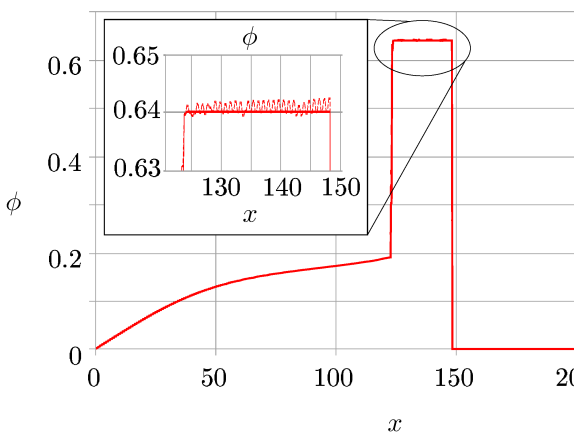

(a) Krieger-Dougherty, $\beta = 1$

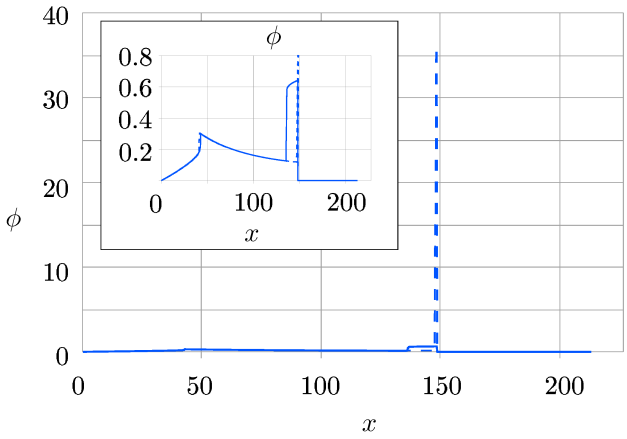

(b) Krieger-Dougherty, $\beta = 2$

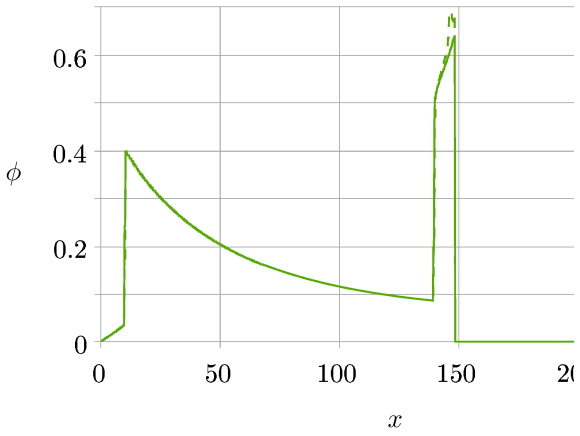

(c) Krieger-Dougherty, $\beta = 3$

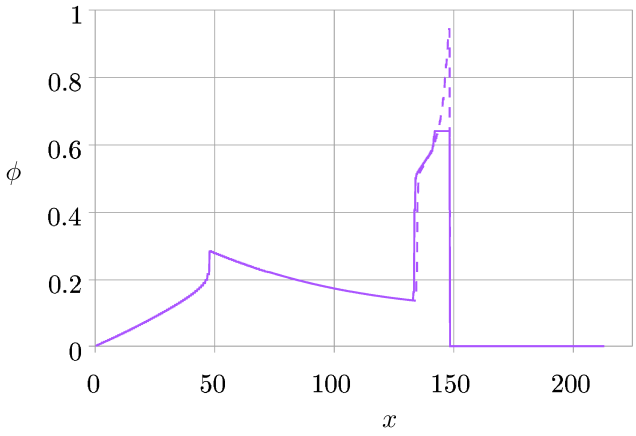

(d) Eskin and Miller

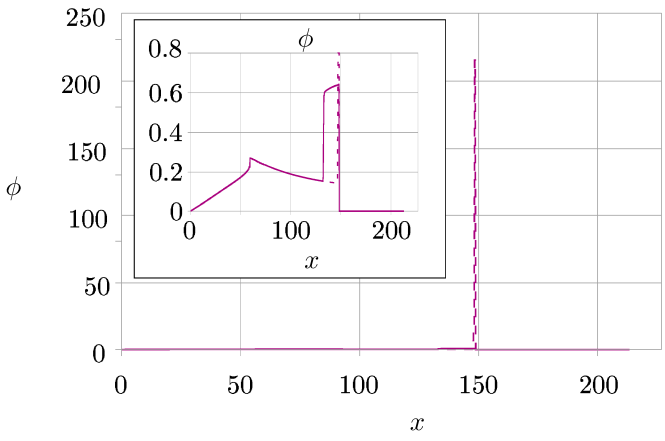

(e) Eilers

Figure 17: Proppant concentration at 1800s using various effective viscosity formulas with (solid line) and without (dashed line) concentration constraints

The numerical method is verified by evaluating the rarefaction wave that occurs as proppant is injected at high concentrations into a fracture and the compression wave that occurs as when a proppant plug is formed at a small fracture width. Proppant advection through an elliptical fracture is investigated, in which proppant bridging is observed at the location where the fracture width is too narrow for proppant to pass. The maximum injection rate permissible before a proppant plug forms at the inlet is calculated using the approximation for the proppant characteristic speed. Finally, proppant transport through a plane-strain KGD fracture is investigated which shows that the steep change in pressure gradient at the fracture inlet causes a build-up of proppant near the inlet, and a narrow fracture width may cause a plug along the fracture before proppant reaches the tip. Solutions are compared using various functions for effective slurry viscosity and it is observed that the Krieger-Dougherty expression with $\beta = 1$ results in the fastest moving proppant, while $\beta = 3$ results in the slowest moving proppant. The other viscosity functions produce results that lie between those extremes.

The results obtained in this work further the understanding of the nonlinear advection of proppant through a fracture. It is of particular importance in grasping the limitations of mixture models where linear proppant advection is performed as a separate step after coupling the rock deformation and slurry flow. More rigorous simulation of the proppant transport mechanisms requires coupling to the slurry flow and rock deformation processes and increasing model dimensions to include the effects of settling. The model presented provides a numerical foundation for simulating the complexities of nonlinear proppant transport.

Acknowledgments

The authors acknowledge the support of Natural Sciences and Engineering Research Council of Canada (NSERC) for their support under a Discovery Grant and the support of an Early Researcher Award from the Ontario Ministry of Research and Innovation.

[1] M. B. Smith, C. Montgomery, Hydraulic Fracturing, CRC Press, Boca Raton, 2015.
[2] J. Adachi, E. Siebrits, A. Peirce, J. Desroches, Computer simulation of hydraulic fractures, International Journal of Rock Mechanics and Mining Sciences 44 (5) (2007) 739–757. doi:10.1016/j.ijrmms.2006.11.006.
URL http://www.sciencedirect.com/science/article/pii/S1365160906001870
[3] E. Detournay, Mechanics of Hydraulic Fractures, Annual Review of Fluid Mechanics 48 (1) (2016) 311–339. doi:10.1146/annurev-fluid-010814-014736.
URL https://doi.org/10.1146/annurev-fluid-010814-014736
[4] G. Hattori, J. Trevelyan, C. E. Augarde, W. M. Coombs, A. C. Aplin, Numerical Simulation of Fracking in Shale Rocks: Current State and Future Approaches, Archives of Computational Methods in Engineering (Jan. 2016). doi:10.1007/s11831-016-9169-0.
URL http://link.springer.com/10.1007/s11831-016-9169-0
[5] B. Lecampion, A. Bunger, X. Zhang, Numerical methods for hydraulic fracture propagation: A review of recent trends, Journal of Natural Gas Science and Engineering 49 (2018) 66–83. doi:10.1016/j.jngse.2017.10.012.
URL https://linkinghub.elsevier.com/retrieve/pii/S1875510017304006
[6] A. A. Osiptsov, Fluid mechanics of hydraulic fracturing: A review, Journal of Petroleum Science and Engineering (May 2017). doi:10.1016/j.petrol.2017.05.019.
URL http://www.sciencedirect.com/science/article/pii/S0920410517304928
[7] E. Novotny, Proppant Transport, Society of Petroleum Engineers, Denver, Colorado, 1977. doi:10.2118/6813-MS.
URL http://www.onepetro.org/doi/10.2118/6813-MS
[8] A. Daneshy, Numerical Solution of Sand Transport in Hydraulic Fracturing, Journal of Petroleum Technology 30 (01) (1978) 132–140. doi:10.2118/5636-PA.
URL http://www.onepetro.org/doi/10.2118/5636-PA
[9] P. B. Gadde, Y. Liu, J. Norman, R. Bonnecaze, M. M. Sharma, Modeling Proppant Settling in Water-Fracs, Society of Petroleum Engineers, 2004. doi:10.2118/89875-MS.
URL http://www.onepetro.org/doi/10.2118/89875-MS
[10] L. Zhou, M. Z. Hou, Y. Gou, M. Li, Numerical investigation of a low-efficient hydraulic fracturing operation in a tight gas reservoir in the North German Basin, Journal of Petroleum Science and Engineering 120 (2014) 119–129. doi:10.1016/j.petrol.2014.06.001.
URL http://www.sciencedirect.com/science/article/pii/S0920410514001466

[11] S. Shiozawa, M. McClure, Simulation of proppant transport with gravitational settling and fracture closure in a three-dimensional hydraulic fracturing simulator, Journal of Petroleum Science and Engineering 138 (2016) 298–314. doi:10.1016/j.petrol.2016.01.002.
URL http://www.sciencedirect.com/science/article/pii/S092041051630002X

[12] M. Vahab, N. Khalili, An X-FEM Formulation for the Optimized Graded Proppant Injection into Hydro-fractures Within Saturated Porous Media, Transport in Porous Media 121 (2) (2018) 289–314. doi:10.1007/s11242-017-0959-0.
URL http://link.springer.com/article/10.1007/s11242-017-0959-0

[13] E. Dontsov, A. Peirce, Slurry flow, gravitational settling and a proppant transport model for hydraulic fractures, Journal of Fluid Mechanics 760 (2014) 567–590. doi:10.1017/jfm.2014.606.
URL http://www.journals.cambridge.org/abstract_S0022112014006065

[14] S. A. Boronin, A. A. Osiptsov, Effects of particle migration on suspension flow in a hydraulic fracture, Fluid Dynamics 49 (2) (2014) 208–221. doi:10.1134/S0015462814020094.
URL http://link.springer.com/article/10.1134/S0015462814020094

[15] B. Kong, E. Fathi, S. Ameri, Coupled 3-D numerical simulation of proppant distribution and hydraulic fracturing performance optimization in Marcellus shale reservoirs, International Journal of Coal Geology 147148 (2015) 35–45. doi:10.1016/j.coal.2015.06.006.
URL http://www.sciencedirect.com/science/article/pii/S0166516215300094

[16] E. V. Dontsov, A. P. Peirce, Proppant transport in hydraulic fracturing: Crack tip screen-out in KGD and P3d models, International Journal of Solids and Structures 63 (2015) 206–218. doi:10.1016/j.ijsolstr.2015.02.051.
URL http://www.sciencedirect.com/science/article/pii/S0020768315001055

[17] C. Detournay, J. Lemos, F. Zhang, Development of a proppant transport logic in 3dec, Applied Numerical Modeling in Geomechanics (2016) 13.

[18] M. Roostaei, A. Nouri, V. Fattahpour, D. Chan, Numerical simulation of proppant transport in hydraulic fractures, Journal of Petroleum Science and Engineering 163 (2018) 119–138. doi:10.1016/j.petrol.2017.11.044.
URL https://linkinghub.elsevier.com/retrieve/pii/S0920410517309336

[19] E. V. Dontsov, A. P. Peirce, A Lagrangian Approach to Modelling Proppant Transport with Tip Screen-Out in KGD Hydraulic Fractures, Rock Mechanics and Rock Engineering 48 (6) (2015) 2541–2550. doi:10.1007/s00603-015-0835-6.
URL http://link.springer.com/10.1007/s00603-015-0835-6

[20] P. A. Varadarajan, P. S. Hammond, Numerical scheme for accurately capturing gas migration described by 1d multiphase drift flux model, International Journal of Multiphase Flow 73 (2015) 57–70. doi:10.1016/j.ijmultiphaseflow.2015.03.002.
URL http://www.sciencedirect.com/science/article/pii/S0301932215000580

[21] R. J. Lorentzen, K. K. Fjelde, Use of slopelimiter techniques in traditional numerical methods for multi-phase flow in pipelines and wells, International Journal for Numerical Methods in Fluids 48 (7) (2005) 723–745. doi:10.1002/fld.952.
URL http://onlinelibrary.wiley.com/doi/abs/10.1002/fld.952

[22] P. S. Hammond, Settling and slumping in a Newtonian slurry, and implications for proppant placement during hydraulic fracturing of gas wells, Chemical Engineering Science 50 (20) (1995) 3247–3260. doi:10.1016/0009-2509(95)00152-U.
URL http://www.sciencedirect.com/science/article/pii/000925099500152U

[23] A. Einstein, Eine neue Bestimmung der Molekldimensionen, Annalen der Physik 324 (2) (1906) 289–306. doi:10.1002/andp.19063240204.
URL http://doi.wiley.com/10.1002/andp.19063240204

[24] J. J. Stickel, R. L. Powell, Fluid Mechanics and Rheology of Dense Suspensions, Annual Review of Fluid Mechanics 37 (1) (2005) 129–149. doi:10.1146/annurev.fluid.36.050802.122132.
URL http://www.annualreviews.org/doi/10.1146/annurev.fluid.36.050802.122132

[25] R. Clifton, J.-J. Wang, Multiple Fluids, Proppant Transport, and Thermal Effects in Three-Dimensional Simulation of Hydraulic Fracturing, Society of Petroleum Engineers, 1988. doi:10.2118/18198-MS.
URL http://www.onepetro.org/doi/10.2118/18198-MS

[26] S. Mueller, E. W. Llewellin, H. M. Mader, The rheology of suspensions of solid particles, Proceedings of the Royal Society A: Mathematical, Physical and Engineering Sciences 466 (2116) (2010) 1201–1228. doi:10.1098/rspa.2009.0445.
URL http://rspa.royalsocietypublishing.org/cgi/doi/10.1098/rspa.2009.0445

[27] G. K. Batchelor, The effect of Brownian motion on the bulk stress in a suspension of spherical particles, Journal of Fluid Mechanics 83 (01) (1977) 97. doi:10.1017/S0022112077001062.
URL http://www.journals.cambridge.org/abstract_S0022112077001062

[28] D. Eskin, M. J. Miller, A model of non-Newtonian slurry flow in a fracture, Powder Technology 182 (2) (2008) 313–322. doi:10.1016/j.powtec.2007.06.027.
URL http://linkinghub.elsevier.com/retrieve/pii/S0032591007003191

[29] H. Eilers, Die Viskositt von Emulsionen hochviskoser Stoffe als Funktion der Konzentration, Kolloid-Zeitschrift 97 (3) (1941) 313–321. doi:10.1007/BF01503023.
URL https://doi.org/10.1007/BF01503023

[30] I. M. Krieger, T. J. Dougherty, A Mechanism for NonNewtonian Flow in Suspensions of Rigid Spheres, Transactions of the Society of Rheology 3 (1) (1959) 137–152. doi:10.1122/1.548848.
URL http://sor.scitation.org/doi/10.1122/1.548848

[31] D. G. Thomas, Transport characteristics of suspension: VIII. A note on the viscosity of Newtonian suspensions of uniform spherical particles, Journal of Colloid Science 20 (3) (1965) 267–277. doi:10.1016/0095-8522(65)90016-4.
URL http://linkinghub.elsevier.com/retrieve/pii/0095852265900164

[32] L. Nicodemo, L. Nicolais, R. Landel, Shear rate dependent viscosity of suspensions in newtonian and non-newtonian

liquids, Chemical Engineering Science 29 (3) (1974) 729–735. doi:10.1016/0009-2509(74)80189-2.
URL http://linkinghub.elsevier.com/retrieve/pii/0009250974801892

[33] S. H. Maron, P. E. Pierce, Application of Ree-eyring Generalized Flow Theory to Suspensions of Spherical Particles, Journal of Colloid Science 11 (1956) 80–95.

[34] R. Barree, M. Conway, Experimental and Numerical Modeling of Convective Proppant Transport, Society of Petroleum Engineers, 1995. doi:10.2118/28564-MS.
URL http://www.onepetro.org/doi/10.2118/28564-MS

[35] I. M. Krieger, Rheology of monodisperse latices, Advances in Colloid and Interface Science 3 (2) (1972) 111–136. doi:10.1016/0001-8686(72)80001-0.
URL http://linkinghub.elsevier.com/retrieve/pii/0001868672800010

[36] K. J. Scott, Hindered settling of a suspension of spheres: critical evaluation of equations relating settling rate to mean particle diamter and suspension concentration, no. 497, Chemical Engineering Research Group, CSIR, Pretoria, 1984, oCLC: 254046774.

[37] I. Garagash, A. Osiptsov, S. Boronin, Dynamic bridging of proppant particles in a hydraulic fracture, International Journal of Engineering Science 135 (2019) 86–101. doi:10.1016/j.ijengsci.2018.11.004.
URL https://linkinghub.elsevier.com/retrieve/pii/S0020722518323097

[38] R. J. LeVeque, Finite Volume Methods for Hyperbolic Problems, Cambridge University Press, Cambridge, 2002. doi:10.1017/CBO9780511791253.
URL http://ebooks.cambridge.org/ref/id/CBO9780511791253

[39] D. S. Bale, R. J. LeVeque, S. Mitran, J. A. Rossmanith, A Wave Propagation Method for Conservation Laws and Balance Laws with Spatially Varying Flux Functions, SIAM Journal on Scientific Computing 24 (3) (2003) 955–978. doi:10.1137/S106482750139738X.
URL http://epubs.siam.org/doi/10.1137/S106482750139738X

[40] E. V. Dontsov, An approximate solution for a plane strain hydraulic fracture that accounts for fracture toughness, fluid viscosity, and leak-off, International Journal of Fracture 205 (2) (2017) 221–237. doi:10.1007/s10704-017-0192-4.
URL https://doi.org/10.1007/s10704-017-0192-4

List of Symbols

Δq	Jump in the proppant volumetric flux
Δt	Length of a time step
Δx	Length of evenly-spaced finite volume cells
$\Delta\phi$	Jump in proppant concentration
$\mu(\phi)$	Effective slurry viscosity
μ_0	Viscosity of the carrier fluid
$\phi(x,t)$	Average volumetric concentration of proppant particles across the fracture width
$\phi_0(x)$	Initial proppant concentration at the start of the simulation
ϕ_i^n	Proppant concentration at center of cell i at time t_n
ϕ_m	Saturated proppant concentration
ϕ_s	Stagnation point–concentration at which the characteristic speed changes sign
$\phi_{i,p}^{n+1}$	Predicted concentration at cell i
ρ	Slurry density
ρ_f	Fluid density
ρ_p	Proppant density
ε_s	Small value used to determine whether the jump in ϕw is approaching zero
$\varphi(r)$	Limiter function

a	Average proppant radius
H	Heaviside step function
N	Number of evenly-spaced finite volume cells
p	Fluid pressure
p_i^n	Fluid pressure at center of cell i at time t_n
Q	Slurry mass flux per unit height of fracture
q	Proppant volumetric flux per unit height of fracture
Q_f	Fluid mass flux per unit height of fracture
Q_p	Proppant mass flux per unit height of fracture
q_s	Proppant volumetric flux corresponding to the stagnation point
$q^+_{correct}$	Correction for the approximation of the flux concentration for cells which have a concentration over the maximum
$q^-_{correct}$	Correction for the approximation of the flux concentration for cells which have a concentration below the minimum
$q^c_{i\pm1/2}$	Corrected proppant flux approximations at the edge of cell i
$q^G_{i\pm1/2}$	Approximation of the proppant volumetric flux at the edges of cell i using the Godunov method
$q^n_{i\pm1/2}$	Volumetric flux entering/leaving cell i at the cell edges
$q^{LW}_{i\pm1/2}$	Correction term in the approximation of the proppant volumetric flux using the Lax-Wendroff method
Q_{inj}	Mass flux of slurry per unit area of fracture injected at the wellbore
q_{inj}	Volumetric flux of proppant per unit area of fracture injected at the wellbore
Q_{sink}	Mass flux of slurry per unit area of fracture leaking off into the formation
$r_{i\pm1/2}$	Slope ratio–ratio of upwind concentration gradient to the gradient at the cell edge
s	Proppant characteristic speed
S^+	Set of cells with a proppant concentration above the maximum (ϕ_m)
S^-	Set of cells with a proppant concentration below the minimum ($\phi = 0$)
$s^n_{i\pm1/2}$	Proppant characteristic speed at the edges of cell i at time t_n
s^n_{max}	Maximum proppant characteristic speed in the domain at time t_n
t	Time
t_n	Time at beginning of time step n
t_{n+1}	Time at the end of time step n
v	Slurry velocity

v^{slip}	Slip velocity–difference in velocity of the proppant and the slurry
v_p	Proppant velocity
$w(x)$	Fracture width
w_i^n	Fracture width at center of cell i at time t_n
x	Distance along the length of the fracture
x_0	Location of fracture inlet
$x_{i\pm1/2}$	Location of the edges of cell i
x_{tip}	Location of fracture tip
y	Distance along the fracture width

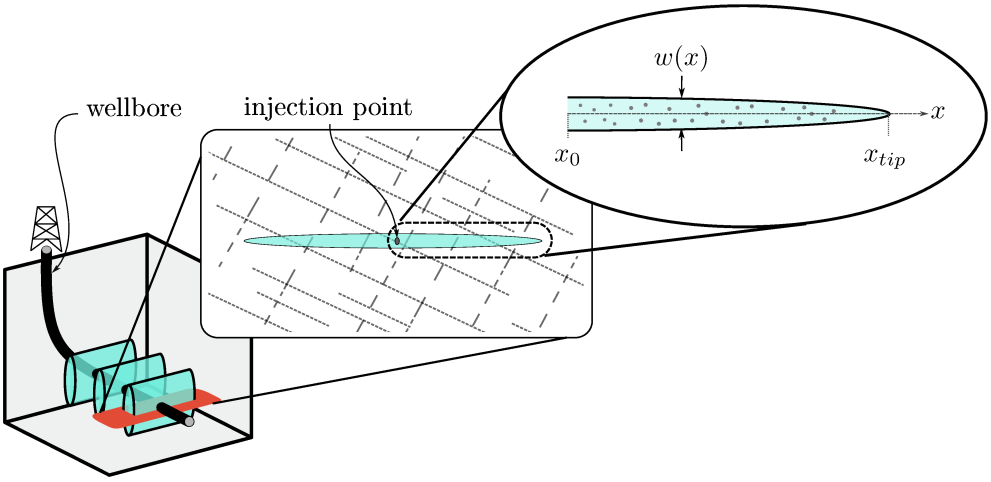

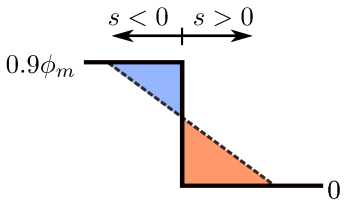

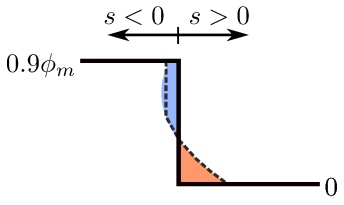

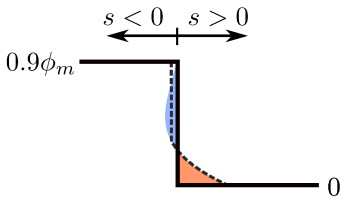

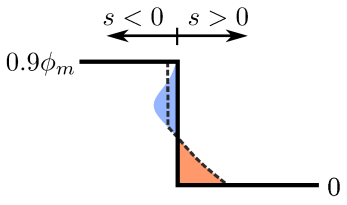

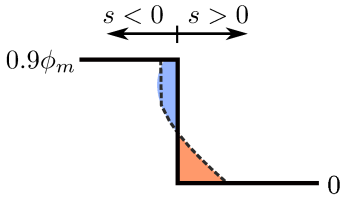

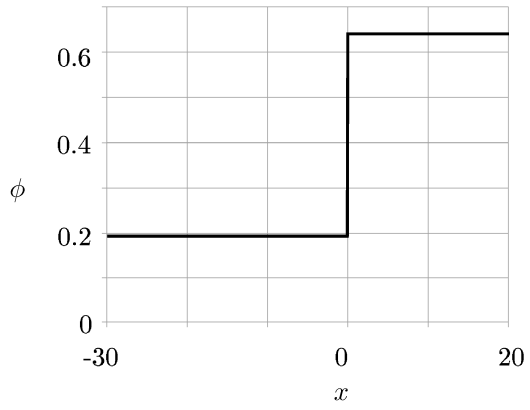

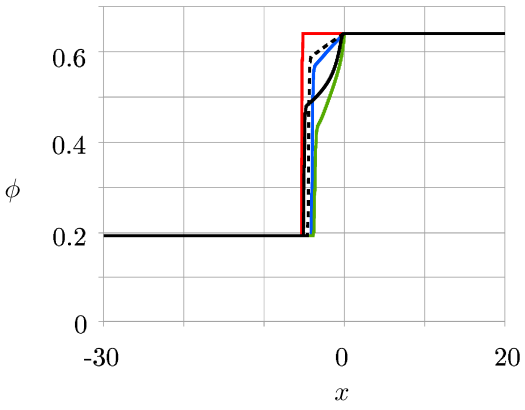

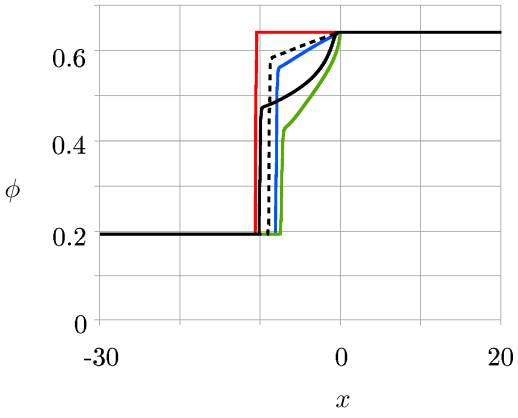

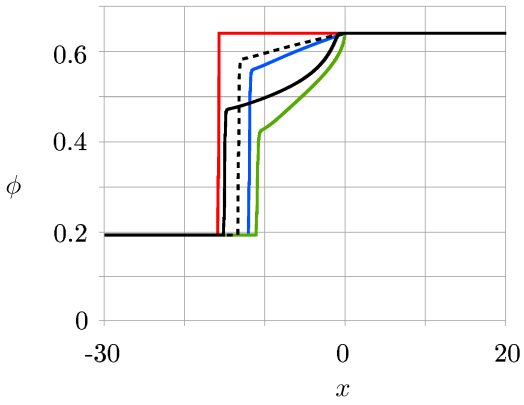

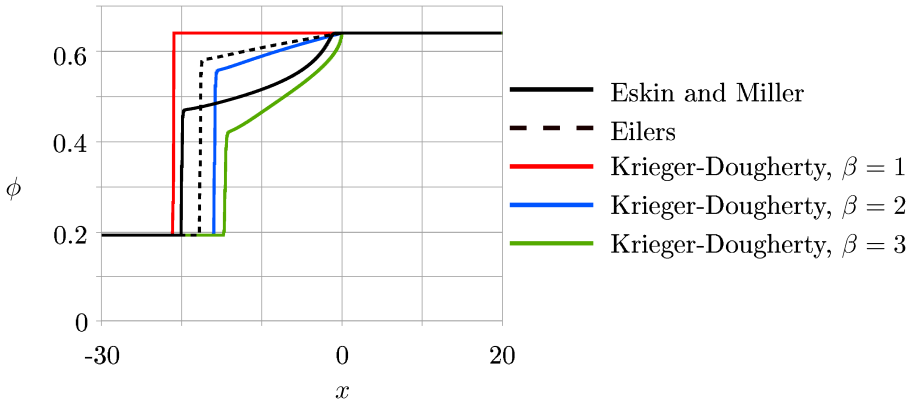

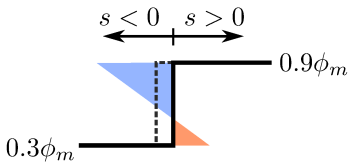

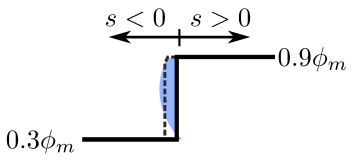

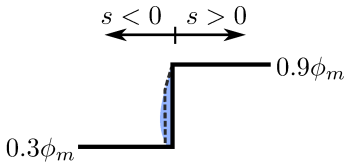

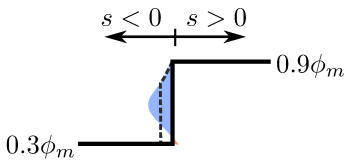

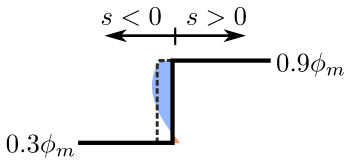

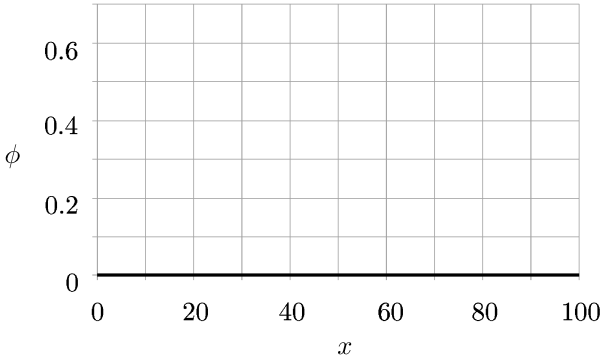

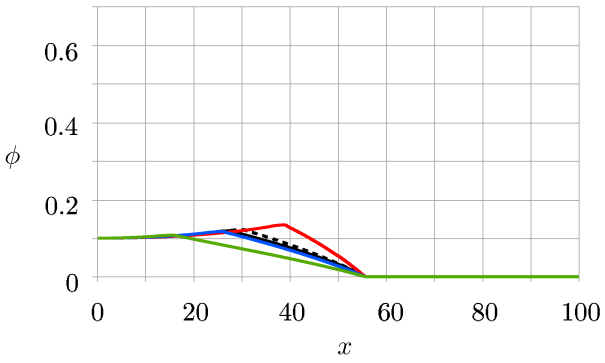

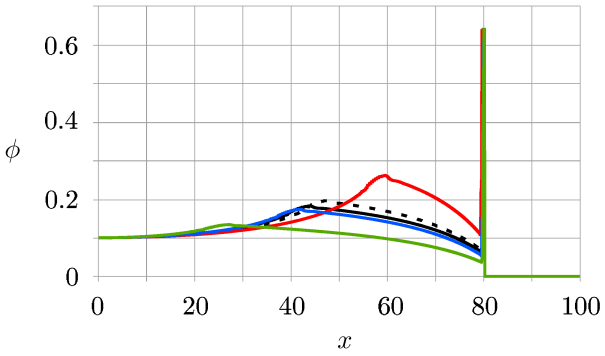

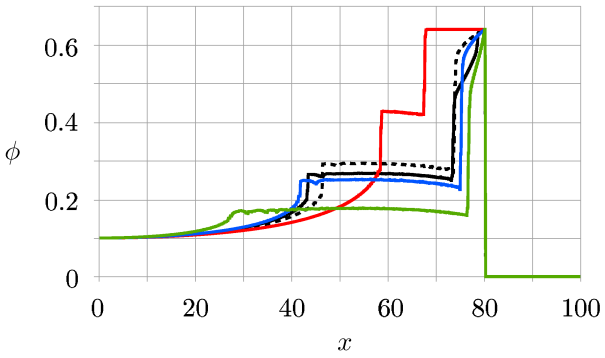

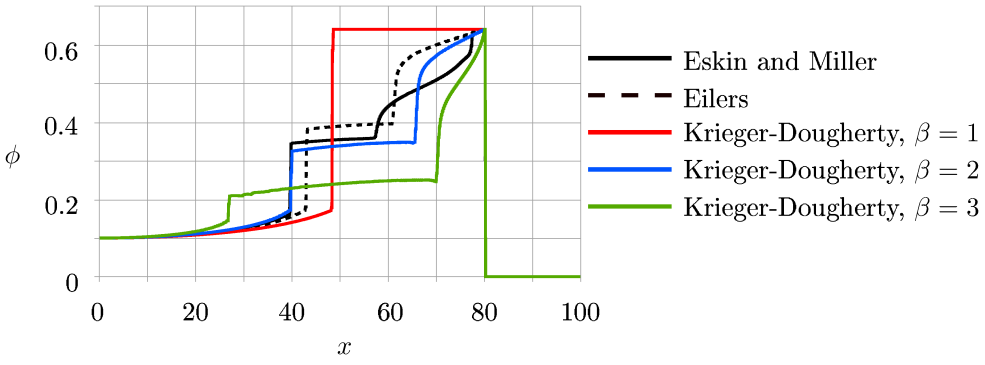

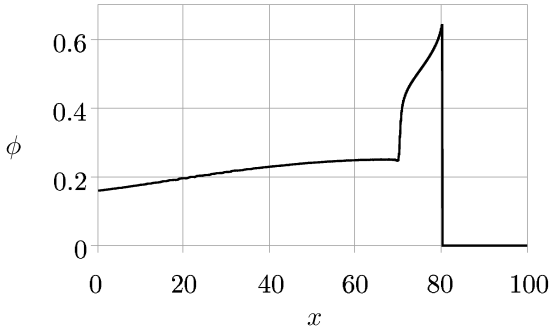

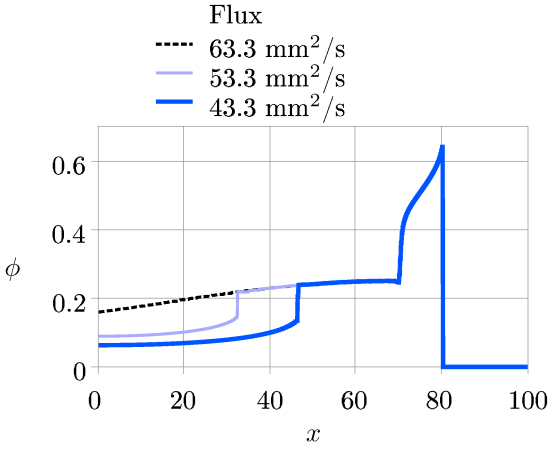

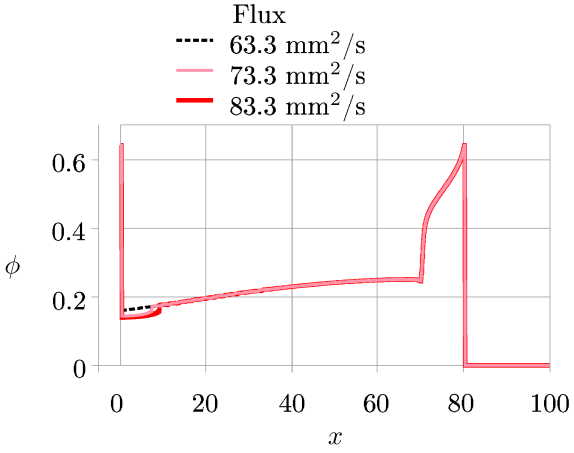

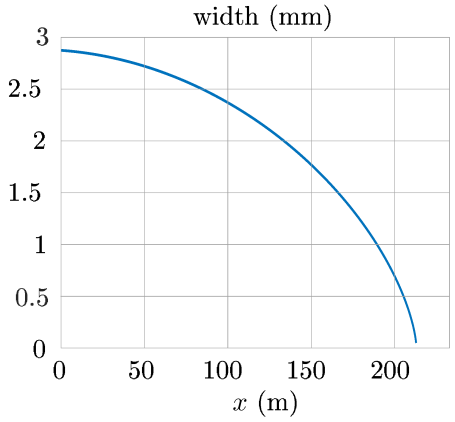

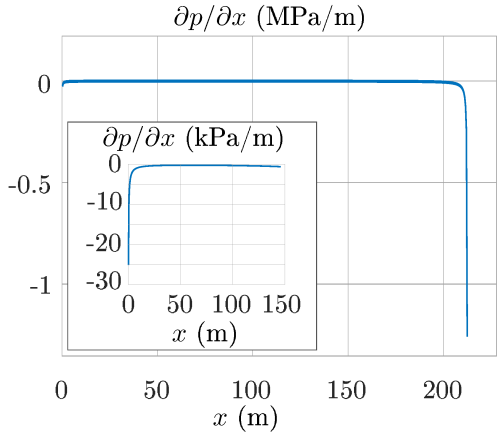

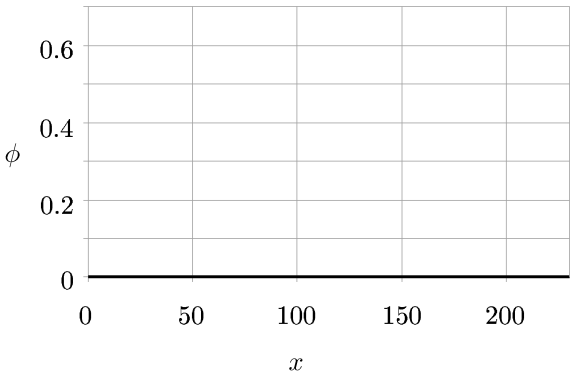

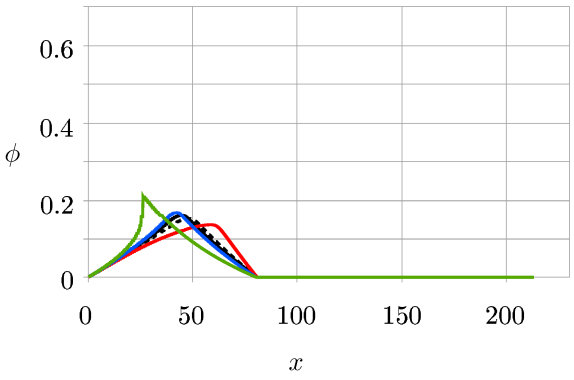

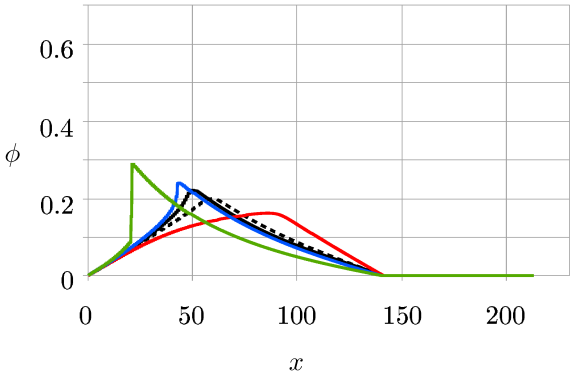

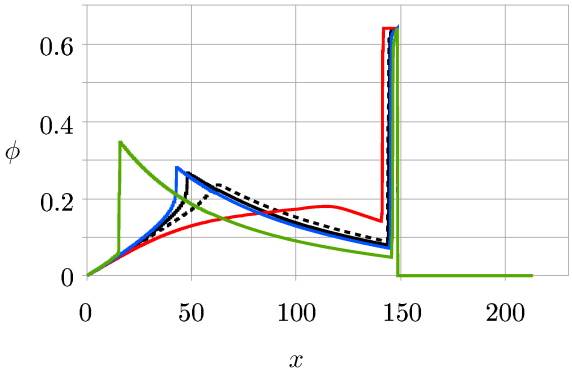

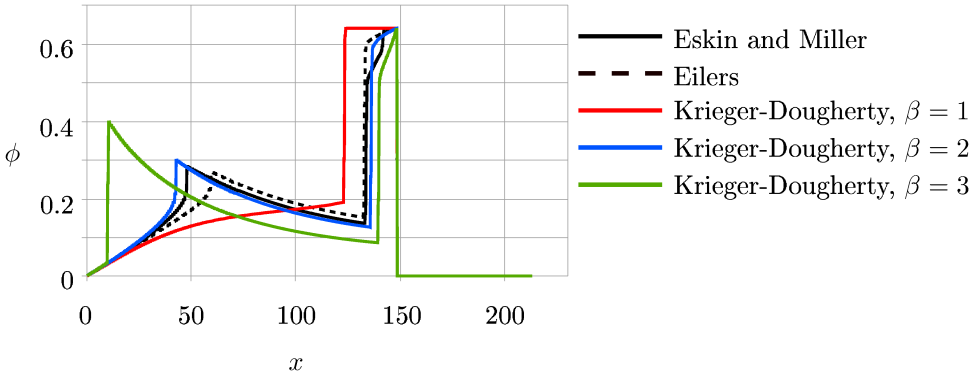

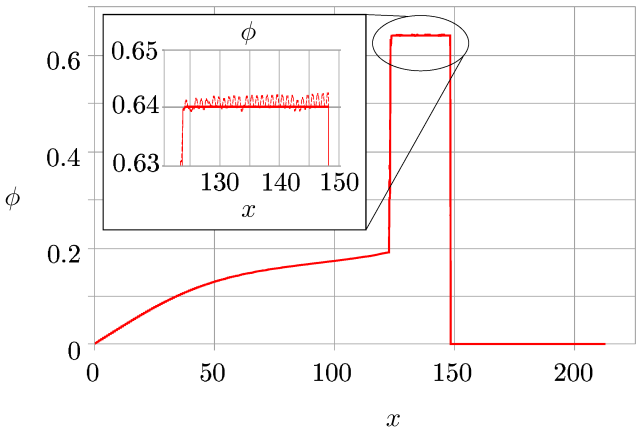

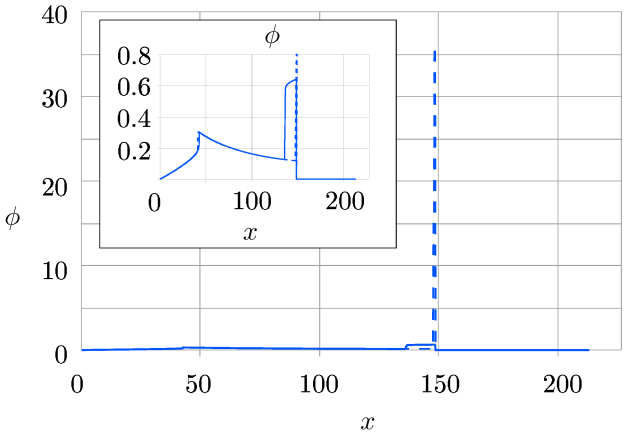

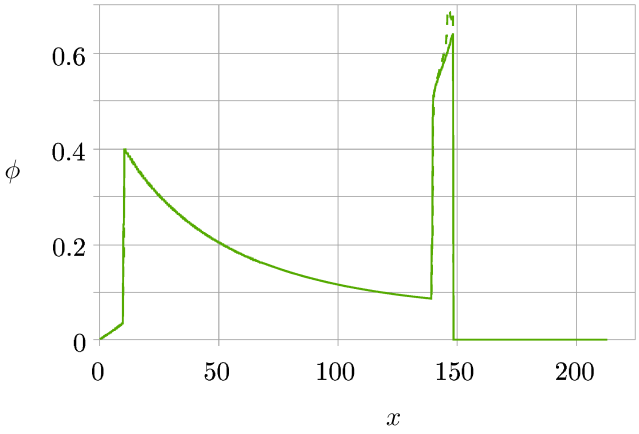

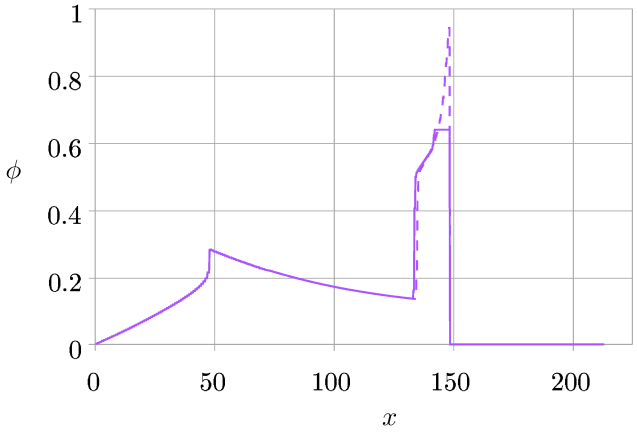

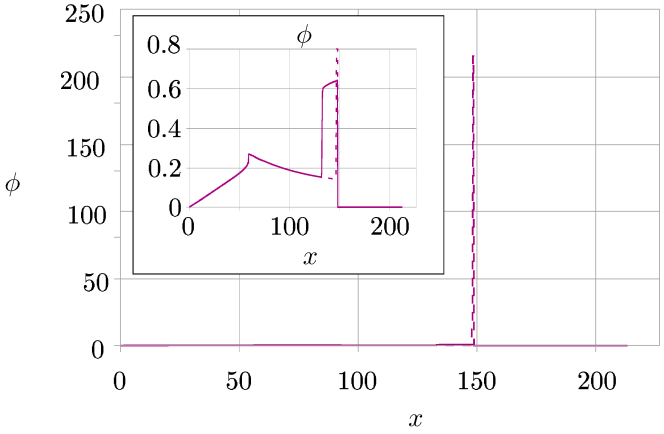

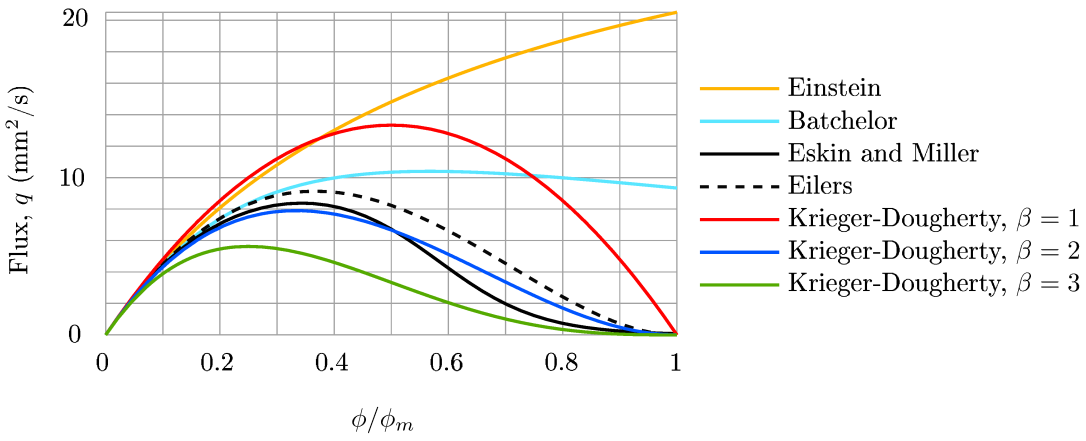

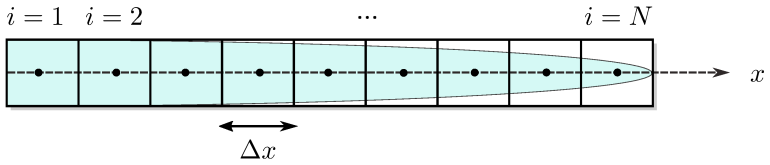

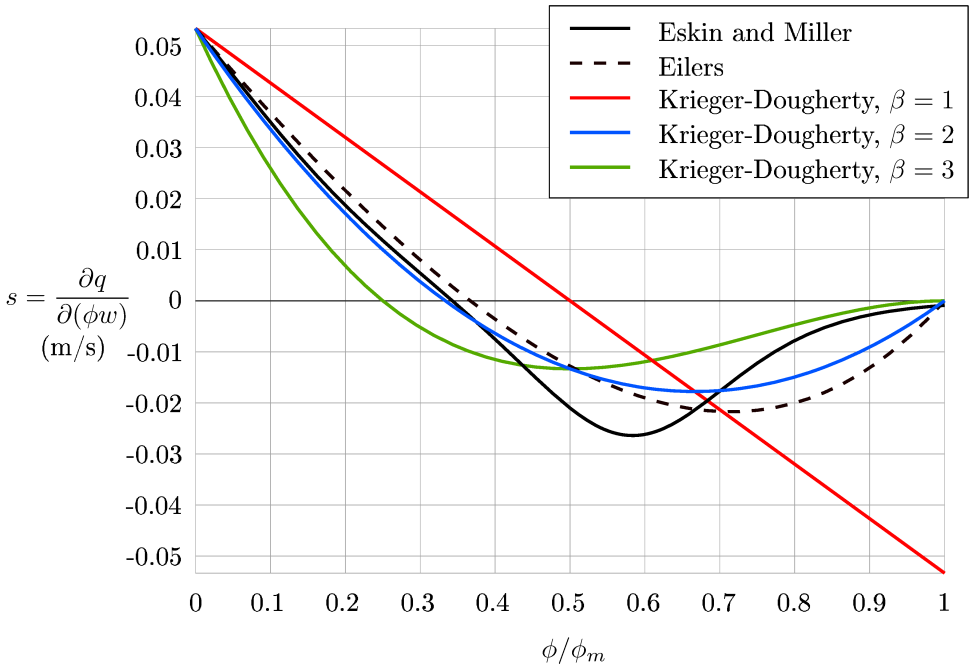

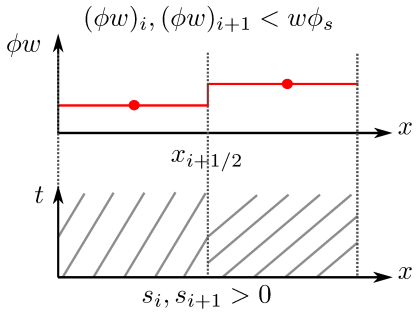

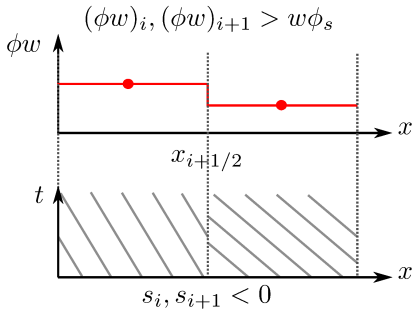

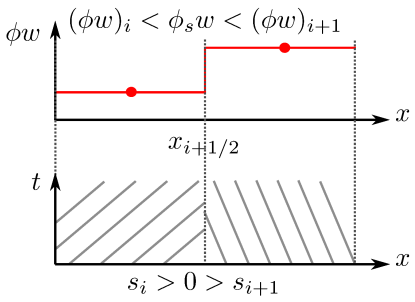

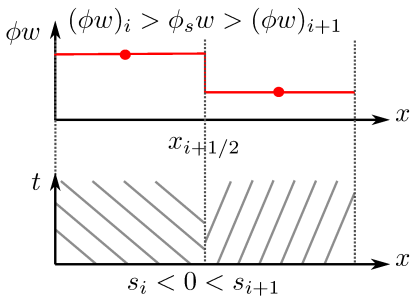

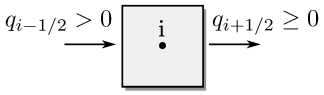

$$q^c_{i-1/2} = q_{i+1/2} - q^+_{correct}$$

$$q^c_{i+1/2} = q_{i+1/2}$$

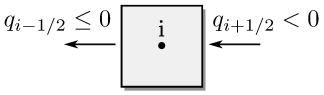

$$q^c_{i-1/2} = q_{i-1/2}$$

$$q^c_{i+1/2} = q_{i-1/2} + q^+_{correct}$$

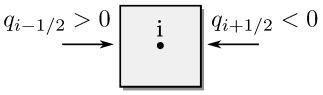

$$q^c_{i-1/2} = \frac{q_{i-1/2}}{q_{i+1/2} - q_{i-1/2}} q^+_{correct}$$

$$q^c_{i+1/2} = \frac{q_{i+1/2}}{q_{i+1/2} - q_{i-1/2}} q^+_{correct}$$

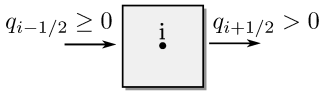

$$q^c_{i-1/2} = q_{i-1/2}$$

$$q^c_{i+1/2} = q_{i-1/2} + q^-_{correct}$$

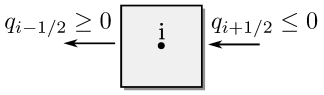

$$q^c_{i-1/2} = q_{i+1/2} - q^-_{correct}$$

$$q^c_{i+1/2} = q_{i+1/2}$$

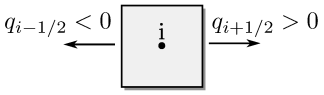

$$q^c_{i-1/2} = \frac{q_{i-1/2}}{q_{i+1/2} - q_{i-1/2}} q^-_{correct}$$

$$q^c_{i+1/2} = \frac{q_{i+1/2}}{q_{i+1/2} - q_{i-1/2}} q^-_{correct}$$

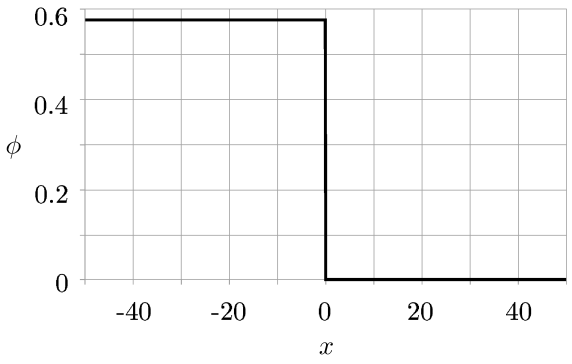

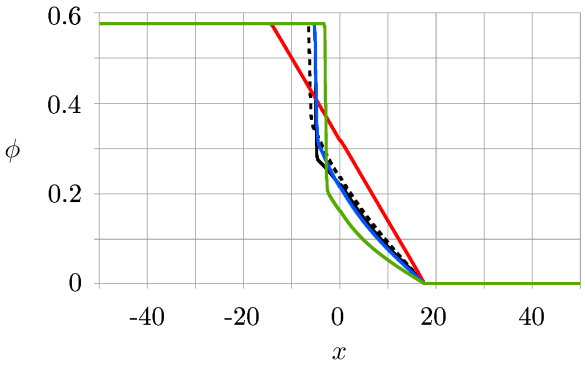

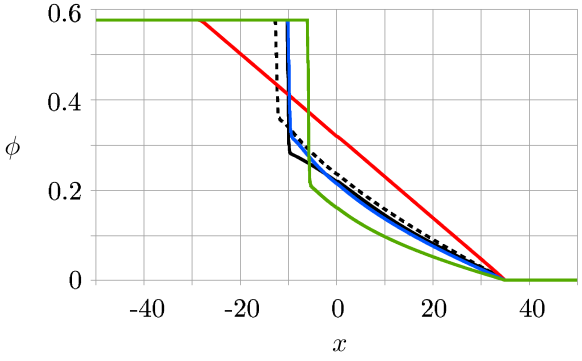

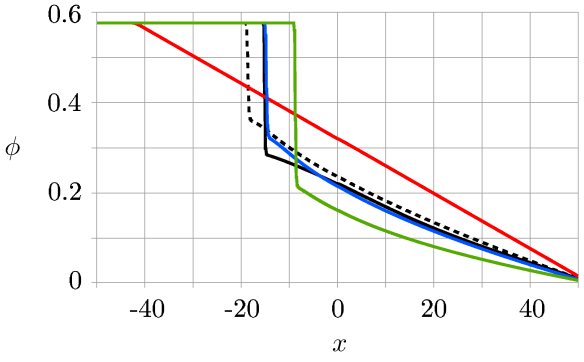

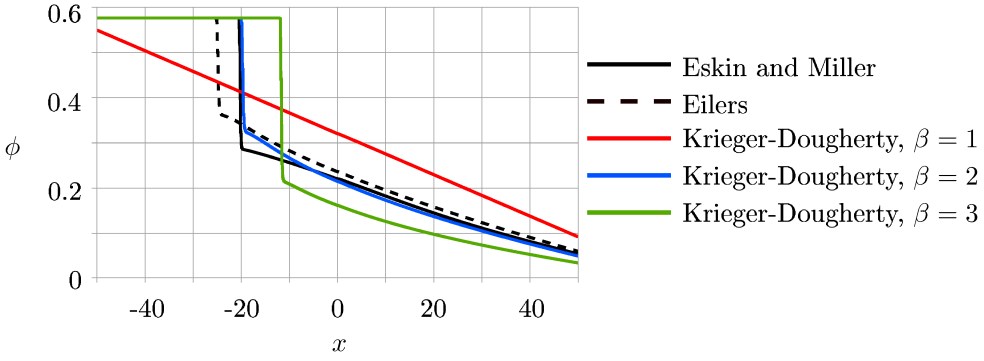

Numerical Considerations for the Simulation of Proppant Transport Through Fractures

Highlights

- The nonlinear hyperbolic equation that describes proppant transport is solved
- Proppant movement depends on the assumed form of the effective viscosity function
- The maximum injection rate before a proppant plug form is calculated
- The Krieger-Dougherty equation using $\beta=1$ results in the fastest moving proppant
- The Krieger-Dougherty equation using $\beta=3$ results in the slowest moving proppant